Lino José Coelho Gonçalves

Transducers for extracellular signal measurements

Faculdade de Ciências e Tecnologia

2017

Lino José Coelho Gonçalves

Transducers for extracellular signal measurements

Mestrado Integrado em

Engenharia eletrônica e telecomunicações

Trabalho efetuado sob orientação de:

Henrique Leonel Gomes

Faculdade de Ciências e Tecnologia

2017

Declaração de autoria de trabalho

Declaro ser o autor deste trabalho, que é original e inédito. Autores e trabalhos consultados estão devidamente citados no texto e constam da listagem de referências incluída.

_____

(Lino José Coelho Gonçalves)

Acknowledgments

In the first place I would like to thank the University of Algarve that gave me, and other students all facilities to make this kind of advanced research possible.

I specially want to thank Professor Henrique Gomes for the opportunity that he gave me to work with him and the huge help that he gave me through all the process of choosing the subject of my thesis, all the research necessary, the work, and the writing, since biology is not my field of study, and here we wanted to make a connection between electronics and biology, without him nothing of this work would be possible. The university of Porto, specially Mónica Cerquido, that produced the devices we studied in this thesis.

I would like to thank specially thank my parents Aida and José that give me this opportunity to study and do a Masters in a science field that I personally like, without them nothing of this work would ever be possible, my sister that always helped me in my education.

I would like to thank my girlfriend Raquel that always supported me all this time since I started my thesis, and never letting me feel the pressure that comes with it.

I would like to thank Pedro Inácio and Ana Mestre that were my colleagues in the laboratory, they helped me a lot during my work and research.

Abstract

The objective of this thesis is to develop and optimize bioelectronic sensing devices for extracellular signal measurements *in vitro*. Ultra-sensitive electrodes were fabricated and electrically characterized. A signal detection limit defined by a noise level of 0.3-0.4 μV for a bandwidth of 0.1 - 12.5 Hz was achieved. To obtain this high sensitivity, large area (4 mm^2) electrodes were used. The electrode surface is also micro-structured with an array of gold and polymer mushroom-like shapes to further enhance the active area. In comparison with a flat gold surface the micro-structured polymer surface increases the capacitance of the electrode/electrolyte interface by six times.

The role of the electrode impedance on the signal quality is discussed in detail. The impedance is modeled by an electrical equivalent circuit and a methodology is presented to extract individual circuit parameters.

The electrode low impedance and low noise enable the detection of weak and low frequency quasi-periodic signals produced by astrocytes populations that thus far had remained inaccessible using conventional extracellular electrodes. Signals with 5 μV in amplitude and lasting for 5-10 s were measured with a peak-to-peak signal-to-noise ratio of 10.

The microstructured electrodes were also used to stimulate electrical activity in glioma cell cultures and astrocytes populations using a train of voltages pulses.

The electrodes and the methodology developed here can be used as an ultrasensitive electrophysiological tool to reveal the synchronization dynamics of ultra-slow ionic signaling between non-electrogenic cells.

Sumário

Esta tese tem o objetivo de desenvolver e otimizar componentes eletrónicos para a deteção de sinais extracelulares *in vitro*. Elétrodos ultrassensíveis foram fabricados e caracterizados eletricamente. O nível de deteção mínimo alcançado foi definido pelo ruído térmico fundamental gerado pelo sensor. Este ruído é de aproximadamente 0,3-0,4 μV para uma largura de banda de 0,1 - 12,5 Hz. Para obter este nível de deteção utilizaram-se elétrodos de grande área (4 mm^2). A superfície do elétrodo também é microestruturada com uma série de formas semelhantes a cogumelos para baixar a impedância do elétrodo. Em comparação com uma superfície plana de ouro, a superfície microestrutura da aumenta em seis vezes a capacidade da interface elétrodo/solução eletrolítica

O papel da impedância do elétrodo na qualidade do sinal é discutido em detalhe na tese. A impedância é modelada por um circuito elétrico equivalente. É também apresentada uma metodologia para extrair os parâmetros individuais que caracterizam o sensor.

O elétrodo de baixa impedância e baixo nível de ruído possibilita a deteção de sinais fracos e de baixa frequência produzidos por populações de astrócitos. Até agora estes sinais permaneceram inacessíveis usando técnicas de medida mais convencionais. Sinais com 5 μV em amplitude e com duração de 5-10 s foram medidos com uma relação sinal/ruído de pico-a-pico de 10.

Os elétrodos microestruturados também foram utilizados para estimular a atividade elétrica em culturas de células glioma e populações de astrócitos.

Esta tese propõe que os elétrodos e a metodologia aqui desenvolvida podem ser usados como uma ferramenta eletrofisiológica ultrassensível para revelar a dinâmica de sincronização da sinalização iónica ultra-lenta (na escala de vários segundos e minutos) entre células não eletrogéneas.

Table of Contents

Index of Figures

1 Introduction

Substrate integrated planar microelectrode arrays (MEAs) are considered the standard electrophysiological methodology for long-term analysis of neurons *in vitro*. MEA technology provides spatial resolution, multi-unit electrical recordings, and a mean for the electrical stimulation of neuron cells. Currently available MEA electrodes have areas typically below 1,000 μm^2 and generate a thermal noise in the range of 5-20 μV. This intrinsic noise defines the system detection limit. In voltage measurements, the electrode thermal noise is inversely proportional to the surface area. Increasing the area of the electrodes causes an increase in sensitivity due to the reduction in noise and impedance. However, as the area increases the ability to discriminate between individual cell signals is impaired. To circumvent this trade-off between electrode sensitivity and spatial resolution several laboratories have started to develop structured electrodes. These emergent electrodes make use of vertical micro or nano-structures coated, namely, with carbon nanotubes, or conducting polymers, which provide a softer and more roughened surface, that increase the contact area between the cells and the electrodes. The strategy behind these approaches is to increase the effective area and to promote a more intimate interaction of the electrode with cells. A well-known example is the use of micron size gold mushroom-like shapes. It has been shown that cells engulf the protruding gold mushroom-like shapes, lowering the impedance and improving the electrical coupling between the cells and the electrode.

Such micro-structured electrodes have been optimized to record action potentials. However, there is some less known electrical activity produced by cells and organs with important physiological/functional roles. This activity generates weak and long lasting electrical perturbations that propagate trough the extracellular milieu. They are caused by ions, and polar molecules or zwitterions that can pass from cell to cell by gap junctions. These fluctuations are steady or slow changing gradients and they progress thousands of times more slowly than action potentials. This activity does not show spikes but smooth signals that can change over a period of time, from several seconds to minutes and often are a result of cell cooperative phenomena. Astrocytes are cells that belong to the central nervous system that generate such type of long lasting signals.

The main goal of this thesis is to fabricate and characterize transducers that can detect signals below one micro-volt. This sensitivity allows us to explore a variety of electrical

communication process used by the astrocytes cells that have been inaccessible using conventional methods.

To achieve a detection limit lower than one microvolt we have to guarantee that the fundamental noise level generated by the electrode is also significant lower than 1μv. This is only possible if large area electrodes are used. However, because of the large electrode area, individual cell signals cannot be resolved, and spatial information is lost. The measured signal is the sum of all individual cell contributions. Uncorrelated cell activity appears as noise. When the cells operate cooperatively, the signal appears as electrical spikes. Therefore, our large electrode layout is optimized to pick up long–time scale synchronized signals from an entire population of cells adhered to the electrode.

The study presented in this thesis describes the electrical characterization of large area electrodes for recording extracellular signals from cells. The cells being studied are glioma cells (an immortal cell line culture) and primary cultures of astrocytes extracted from the brain of a mouse. The electrodes were used both to record signals as well as to electrically stimulate the cells in *vitro*.

This thesis is organized in 7 chapters. After this introduction, Chapter 2 provides a state-of the-art of the current technology for electrophysiological measurements *in vitro*. Chapter 3 introduces the equivalent circuit model that describes the sensing interface. The equivalent circuit developed, allows us to understand how the signal generated by the cell is coupled to the electrode. In particular shows which electrode physical parameters have to be optimized to achieve signal detection with maximum SNR ratio. Having established an equivalent circuit model that describes the sensor it is important to have a methodology to extract the relevant parameters. This procedure for parameter extraction is presented in Chapter 3. The extraction of the individual circuit parameters is carried-out by using three types of measurements (a) small-signal impedance measurements, (b) circuit transient response and (c) by quasi-static methods. The parameter extraction can be used to select the best materials for sensing electrodes and/or to optimize the electrode design. Chapter 5 describes the use of the electrodes as electrical stimulator as well as recording electrode. The electrodes establish a bidirectional communication interface with the living cells. The methods presented and discussed in Chapter 3 are then used on Chapter 4 to evaluate the electrical characteristics of electrodes coated with micro-mushrooms. The performance of these electrodes is demonstrated by measuring ultra-week signals generated by astrocyte populations. Chapter 6 describes long term spontaneous activity of astrocyte showing amplitude modulated (AM) patterns as well as frequency

modulated (FM) patterns. Finally, in Chapter 6 the major findings of this work are summarized and discussed. Suggestions for the continuation of the work are also proposed in Chapter 7.

2 Transducers of cellular electrical signals: A Review

Abstract

This chapter provides a review of the state-of-art on devices to record extracellular signals. Presents the equivalent electrical circuit models. Discuss the impact of the thermal and 1/*f* noise generated by the electrodes on the quality of our measurements. Provides guidelines for the optimization of the electrode for electrophysiology measurements.

2.1 Introduction

The bio-electronic research field started in 18th century, with the experiments of Italian physicists Luigi Galvani and Giovanni Aldini on what at that time was called animal bioelectricity [1]. However, only in 1952 Alan Lloyd Hodgkin and Andrew Huxley laid the foundation of modern electrophysiology with their groundbreaking work on the modeling of action potentials propagation in the squid's giant axon [2]. The modern neuroscience was born with the advances in the fabrication techniques, allowing the realization of glass microelectrodes [3] and the consequent development of the patch-clamp technique through which it was possible to resolve the current of a single membrane channel [4].

The patch-clamp technique gave us a close insight on how the membrane ion channels works. However, despite its numerous features, this tool has a several limitations. In fact, with such a technique it is almost impossible to investigate more than few cells at the same time. It means that, using patch-clamp, the dynamics of cell aggregates cannot be resolved, and with the advent of modern neuroscience this approach became therefore limiting.

This chapter is dedicated to the way in which the technology has evolved during the last 40 years. Particular attention will be drawn to the most used devices for the transduction of extracellular signals, namely the Micro Electrode Arrays (MEAs) and the Field Effect Devices (FEDs). The use of new emergent nanomaterials will also be reviewed.

We start by reviewing the models of the electrolyte/sensing device interface. Particular attention is paid to the parameters that control the electrical coupling between the bio-signals generated by the cells and the sensing electrode or device. How the electrical noise affects the quality of the measurements is also addressed.

2.2 Extracellular electrophysiological measurements

2.2.1 Terminology and basic concepts

Here we review some basic concepts and terminology, for instance, we define what is an extracellular signal, or a monophasic signal. An extracellular recording involves placing one electrode in close proximity to the cell and the reference electrode at some location in the extracellular fluid. This arrangement records potential changes at the membrane surface rather than across the membrane.

Action potentials recorded extracellularly differ from those recorded intracellularly in several important aspects. The size of any action potential will be obviously reduced. The shape of the waveform for any one action potential will depend on the exact geometry of its contact with the electrode. Extracellular techniques are therefore better suited where one only wants to know that an action potential has occurred or to record the activity of an entire population of cells.

Both the classic intracellular action potential and the extracellular action potential are biphasic. In other words, they have both positive and negative deflections, but for different reasons. The negative phase of the intracellular action potential is attributed to the mechanism of after-hyperpolarization. The negative phase of the extracellular signal is due to the manner in which it is recorded, which will be explained below.

There are two wire recording electrodes (R1 and R2 as shown in Fig. 1) touching the nerve, each connected to one input of the differential amplifier. The shape of the extracellular signal depends on the position of the two electrodes with respect to the travelling signal. Before the stimulus is delivered, both wires should be measuring basically the same voltage. There will be no deflection recorded because the amplifier takes the difference of the two inputs before passing the signal on to the A/D converter. The situation changes as the extracellular signal travels along the nerve. The shape of the extracellular signal will depend on the relationship between the inter-electrode distance, the length of the axon segments depolarized by the action potentials, and the conduction velocities of the axons. When the extracellular signal has reached the first recording electrode (R1, proximal), the proximal electrode becomes transiently negative to the distal electrode; the potential difference between the two is detected and the trace is displayed as an upward deflection.

As the signal progresses between both recording electrodes, the recorded potential returns to the base line (no voltage difference between the two recording electrodes). As the signal passes the second electrode (R2), a deflection of the same size but opposite sign will be recorded. The sign is negative because of the way the amplifier compares the two inputs.

If the electrodes are not separated by a large distance, the two phases will not be of equal amplitude. The signal will not have completely passed the first electrode before reaching the second. Adding the two opposite signed deflections will reduce the amplitude of the negative phase and decrease the apparent width of both deflections.

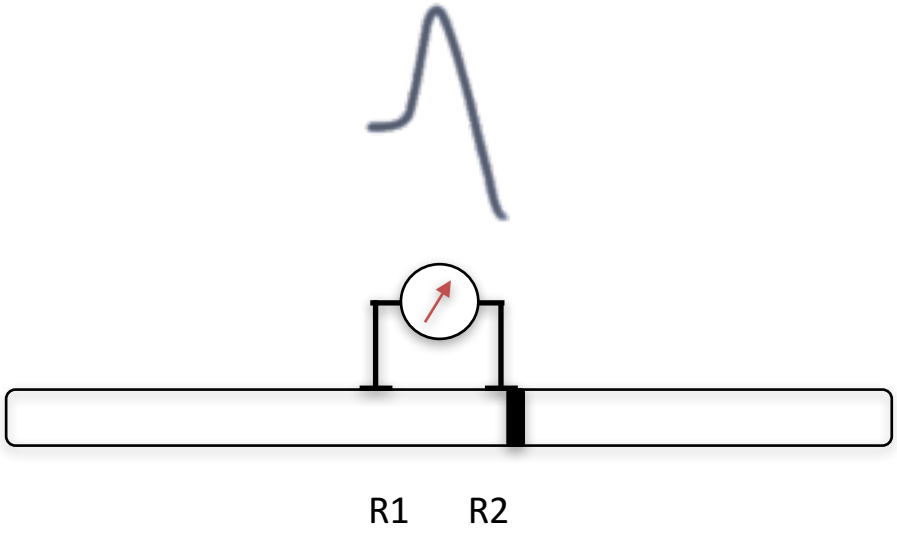

Fig. 1: This figure shows what we measure as the signal travels from R1 to R2.

2.3 Modelling of the cell/device interface

2.3.1 The metal-electrolyte interface

In order to understand the mechanisms behind the extracellular transduction of an bioelectrical signal by means of metallic or semiconductive electrode, it is crucial to understand what happens at the electrode/electrolyte interface. When a metal or a semiconductor is immersed inside an electrolyte solution the surface becomes polarized. Positive ionic charges appear at the surface of the metal. These distributed positive charges are compensated by a sheet of negative charges on the metal. This interfacial polarization is known as electrical double-layer (EDL). Fig. 2 shows a schematic representation of the interfacial polarization effect. A double-layer is essentially a molecular dielectric and stores charge electrostatically. From an electrical point of view an EDL behaves as a capacitor. Because the EDL is usually

formed by a charge distribution of ions as a function of distance from the metal surface allows it can be modelled by two capacitors in series as shown in Fig. 2. The diffusion capacitance (C_{diff}) is usually small and can be neglected.

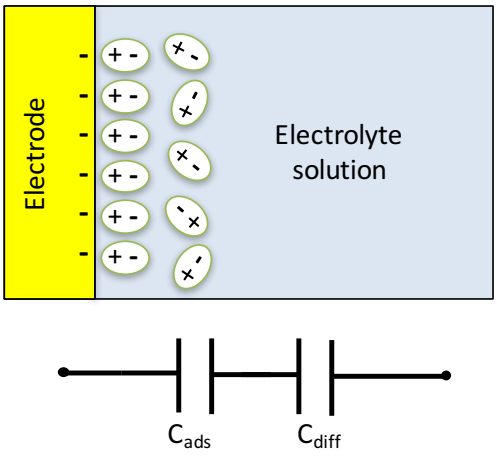

Fig. 2: Schematic representation of an electrical double-layer. The figure also shows that the electrical double-layer can be described by two capacitors in series, usually C_{diff} is relatively small and can be neglected.

Depending on the type of electrode material, two different phenomena may happen when the electrode is put inside an electrolyte solution and connected to a voltage source: either a current will flow through the circuit (thus the potential at the electrode/electrolyte interface does not change by changing the voltage), or no current will flow through the circuit (in this case a charge separation at electrode/electrolyte is obtained and the surface potential will follow exactly the voltage source variations). According to these two possible behaviors, electrodes are classified as not polarizable (as in the first case) and polarizable (as in the second case). The words non-Faradic (for non-polarizable) and Faradic electrodes are often used in the literature. A schematic representation of this classification is shown in Fig. 3. Of course, in real applications the distinction between polarizable and not polarizable electrodes is not as sharp as it is in theory (in fact, only mercury can be considered a perfect polarizable metal, and only in a limited range of polarizations). A generally accepted way to describe the behavior of an electrode in contact with an electrolyte is to model it as the parallel between a capacitor (which models the extent to which the electrode is polarizable) and a resistor (which takes into account the presence of Faradic currents).

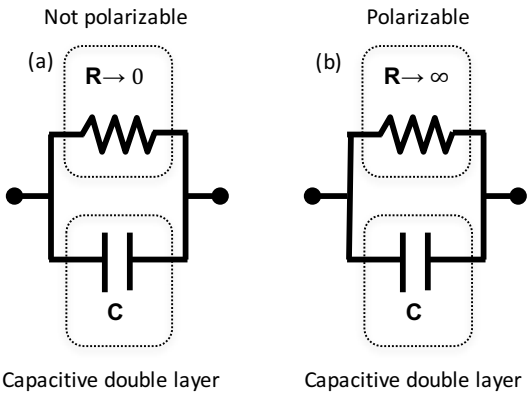

Fig. 3: Graphic representation of the double nature of the electrode/electrolyte interface, modeled as a RC circuit. An electrode is considered not polarizable when R → 0 (a), and polarizable when R→∞ (b).

The electrical double-layer is the sensing layer and not the electrode. The EDL capacitance and the resistance have an important role in the signal transduction. The signal path is through the lowest impedance element, the capacitor. It is then convenient that the capacitance is as high as possible to offer the lowest impedance to the signal. The parallel resistance basically generates noise and degrades the signal-to-noise ratio.

Different materials establish different EDLs. Metals such as gold establish polarizable EDLs. In contrast, conducting polymers based electrodes establish a EDL with a low interfacial resistance.

The noise generated by the EDL resistance can have two components depending if the interface behaves as polarizable electrode or not. If the resistance is very high, it may only generate thermal noise. However, if the interfacial resistance is low as in the case of conducting polymer based electrodes, the current passing through the resistance may generate also shot noise that will add to the thermal noise.

2.3.2 Electrical models and equivalent circuits

The cell/electrode interface can be modeled by a relatively simple electrical model. The extracellular action potential transduction depends in fact only on few parameters with which it is possible to precisely control the cell/electrode coupling [5]. In Fig. 4 a typical model for the neuron/planar microelectrode coupling is shown. By referring to Fig. 4 the parameters involved in the model are:

• C_D . Is the double-layer capacitance.

• R_{seal} is the sealing resistance. It models the way in which the cell adheres to the electrode surface.

• R_C is the spreading resistance. It is perpendicular to the cell membrane and the electrode surface. It models the signal loss due to the cell-electrode distance.

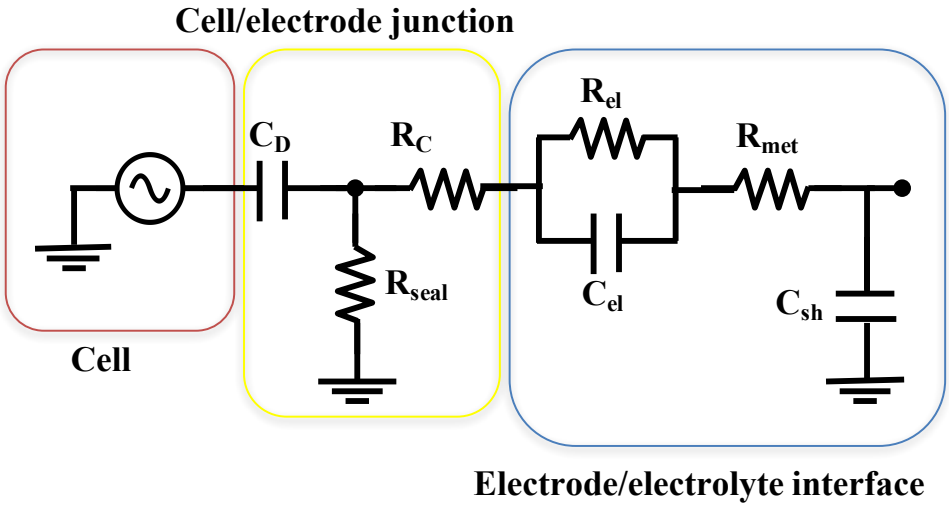

Fig. 4: Equivalent circuit of an electrode-neuron interface.

Both point/area contact circuit models, that assume a tight seal between the cell and the electrode, and circuit models that consider the detection of the electrical activity of cells that are not in tight contact with the electrode, have been considered [5]–[12]. These circuit models are helpful to interpret how charge fluctuations generated by a cell are coupled into the sensing electrode and how they are measured either as voltage or as current signal. Charges passing through the channel pores at the cell membrane create regions of charge excess/depletion giving rise to potentials that can be detected at different points. A simplified point/area circuit model based is shown in Fig. 5. This circuit describes a physical situation where there are two electrodes. One of the electrodes acts as measuring electrode, and the other as a counter-electrode. R_D and C_D are the resistance and capacitance, respectively, of a simplified model of the electric double-layer that forms at the electrode-electrolyte interface. This circuit is a reduction of the more complex model, consisting of a constant-phase-angle impedance and charge-transfer resistance. For the sake of simplicity these elements are not included in the model of Fig. 5. Without cells, when we look across the two electrodes the high impedance double layers appears effectively in series with the low impedance electrolyte layer described by a resistance R_S and a capacitance C_S. When cells are in contact with the measuring electrode,

the signal loss between cell and the measuring electrode is modeled by the resistance R_C. It is important that $R_C \ll R_S$, this ensures that the extracellular signal is essentially coupled into the measuring electrode.

The electrolyte impedance in series with the counter electrode double- layer impedance represents what is called the seal impedance Z_{Seal}. The seal impedance is defined as the resistance between the cell and the surrounding solution (ground).

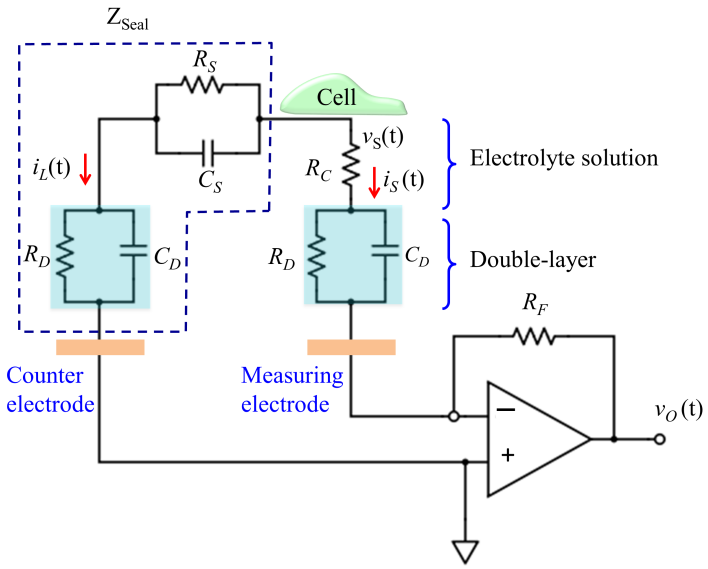

Fig. 5: Schematic diagram representing the electrical coupling between the cell and the measuring circuit. A trans-impedance differential amplifier is used. The amplified signal is $i_s(t)$ *[51]*.

2.4 Noise in electrophysiological measurements

In the most general sense, noise can be defined as any disturbance that interferes with the measurement of the desired signal. In electrophysiological measurements, such disturbances can arise from the preparation itself, the electrodes that couple the preparation to the measurement instrument, the electronic instrumentation, interference from external sources (e.g., electrostatic and electromagnetic coupling between the circuitry and 50 Hz power lines, fluorescent lights, video monitors, and noise associated with mechanical vibrations), and, if the data is digitized (as is usually the case), from the digitization process itself (e.g., quantizing noise).

We will begin by discussing the basic noise mechanisms that arise from the physics of the materials and devices that comprise the electrical system. Interference from external sources and noise associated with digitization will not be considered. The main fundamental types of noise are: thermal noise, shot noise, and "excess" noise (e.g., 1/*f* noise). These types of noise form the basis for a discussion of amplifier noise and electrode noise.

All the fundamental types of noise are completely random in nature. Their average properties can be measured, but their actual values at any particular instant in time cannot be predicted. One of the most convenient methods to measure the amplitude of noise is its root-mean-square (rms) value [13].

When considering noise in the time domain, it is important to know the bandwidth over which the noise process is observed. The Noise is made up of many frequency components, frequently extending from D_C to many mega-hertz or giga-hertz. Some noise processes are naturally restricted in bandwidth, but most require the appropriate use of filtering to restrict the bandwidth of the noise while allowing adequate resolution of the signal. When a noise amplitude (rms or peak-to-peak) is discussed, it is appropriate to also note the bandwidth over which the noise is observed and the type of filter that has been used to restrict the bandwidth.

2.4.1 Excess Noise

Excess noise can be broadly defined as any noise that is present in a circuit element in addition to the fundamental noise mechanisms already described. For example, in the presence of direct current all resistors exhibit low-frequency noise whose power spectral density varies inversely with frequency. This noise is usually referred to as “1/*f* noise”.

2.4.2 The cell-electrode interface noise model

Typically, when there is no net current flowing through the interface, which corresponds to no charge transfer process present at the interface ~ i.e., non-Faradaic electrodes, only thermal noise is anticipated. Hence, the spectral density of the measured noise relies on the macroscopic equivalent circuit model of the setup, and its possible frequency dependencies. Conversely, in the case in which charge transfer occurs at the interface, a current-dependent fluctuation becomes apparent ~ i.e., shot noise, in addition to incessant thermal noise, originating from all dissipative components. Shot noise can be observed as a consequence of

the current passing through the circuit, where the flow of electrons suffers attenuations. These changes, are observed as current fluctuations in the time domain. Also, they are mostly originated by slow processes (in the order of seconds to minutes), meaning that in the spectrum, it will be observed changes in the low frequencies tail.

The excess shot noise is inherently frequency dependent, and its spectrum is denoted by the charge transfer and mass transfer processes of the electro-active species, in proximity of the interface. If the mass transfer process is dominated by electric field effects, the noise spectra possess a $1/f^2$ dependency, while in diffusion-dominant electrodes, ionic relocation can potentially bring about excess noise obeying an inverse frequency power law ~ i.e., $1/f$ noise.

2.5 Microelectrode arrays (MEAS)

MEAs, at the moment, represent the gold standard for extracellular monitoring of electroactive cells aggregates, because of their well consolidated transduction principle and the possibility to record and electrically stimulate cells, both *in vivo* and *in vitro*. Standard materials for MEAs fabrication are Pt, Au, Irx and Indium Thin Oxide (ITO) for the electrodes, and Si4N4, EPON SU-8 and polyimide for the passivation layer. Another important peculiarity of the MEA approach is the possibility to perform-long term recordings (up to several months for *in vitro* applications), with high stability and good reliability.

Classic MEAs are typically embedded in glass substrates. Nevertheless, during the last years, several kinds of innovative materials have been investigated in order to realize mechanically flexible MEAs for both *in vivo* (such as polyimide based [14], 3D flexible MEAs [15], and all-polymer MEAs made of Poly(3,4-ethylenedioxythiophene) Polystyrene sulfonate—PEDOT:PSS, an organic semiconductor), and *in vitro* applications (such as for example Polydimethylsiloxane-based devices [16]). More recently, an interesting approach for an easy-to-fabricate Microelectrode Array based on a conducting polymer has been proposed by Sessolo et al. [17]. The flexibility is a very important feature dealing with bio-applications, because of the huge differences in terms of mechanical properties between intrinsically “soft” living tissues and conventional materials for recording electrodes. This mechanical incompatibility is strongly related to the so-called foreign-body response (especially *in vivo* applications), and this undesired effect must be minimized in order to obtain reliable and long-lasting bio-electronic interfaces, otherwise the body can reject the electrodes causing some kind of inflammatory reaction.

As previously highlighted, MEAs constitute a very important tool in neuronal networks studies, since this kind of devices are able to perform long-term recordings on electroactive cells and to elicit responses through electrical stimulations, both *in vivo* and *in vitro*. During the last decades, a huge amount of effort has been directed to improve the performances of such devices. In particular, bioMEMs (bio Micro Electro-Mechanical systems) integration allowed the realization of more and more complex structures, such as the so-called neuro-cages [18], or particular micro-structures for neuronal networks patterning [19], [20].

Despite the enormous effort and the undeniable advances, classic MEAs still suffer from several drawbacks such as high impedance (which limit the scale down of the recording sites), the current shielding phenomenon [21], and the difficult management of the external wiring, making it difficult to obtain high-density MEAs. For example, for a standard neuronal *in vitro* application, it is easy to have more than 50,000 neurons against up to few hundreds recording sites, and this results in a high spatial under-sampling of the culture's activity.

In order to overcome the problems mentioned, CMOS technology has been introduced in the realization of a new family of MEA devices with a high recording sites density and on-chip signal conditioning (such as, for example, pre-amplification stages, AD conversion, and multiplexing), thus reducing the external wiring complexity and some of the external noise sources. Representative examples of a CMOS device for neurophysiological applications are the so called Michigan probes [22], a widely employed tool for in *vivo* applications, and the chip proposed by Heer et al. [23], which was able to record from 128 electrodes with a sampling frequency of up to 20 kHz. Another interesting approach involving CMOS technology is the Active Pixel Sensor approach (APS—this method was originally conceived for video applications [24]). In 2005, Berdondini et al. [25] developed an APS-MEA for *in vitro* applications, consisting of 64x64 pixels on an active surface of 2.5mm^2.

2.6 Nanomaterials and devices for extracellular recording

2.6.1 Electrolyte gated field-effect transistors

A different approach to extracellular measurements stems from the silicon technology. The introduction of an integrated-circuit approach to microelectrodes in 1970 [26] marked the beginning of a new paradigm in the way to interface with living matter. In the same year, Bergveld, with his famous letter [27], first proposed a completely new device for neurophysiological measurements called Ion Sensitive Field Effect Transistor. The full paper on the same topic was published two years later [28], and consolidated the ISFET theory, thus laying the foundation of a completely new field of research based on the exploitation of field effect devices for the transduction of extracellular biopotentials.

In the following years, tens of studies deepened the ISFET working mechanism and extended its applicability to different kinds of sensing applications (since, as Bergveld himself further confirmed, the ISFET device was specifically conceived as an electrophysiological tool), from cell metabolism monitoring both in *vitro* [29], [30] and *in vivo* [31] to the sensing of different enzymes and ions concentration.

Two important models of the FET-cell interface have been elaborated, namely the Bergveld model and the Fromherz model. Both of them describe the interaction between an electrogenic cell and a transistor in an open-gate configuration, which means that the cells are directly cultured onto the gate oxide of a transistor (no gate metallization is present). An alternative approach is represented by the employment of extended gate structures. This approach has, several advantages with respect to the open-gate approach, since the transistors channels are physically separated from the culture region.

In extended gate transistors, each microelectrode can be either directly connected to the gate of a FET [32] or realized using a floating gate approach [33]. In the last approach, the cells are cultured onto the thin insulation layer of an elongated gate that is left floating. As an example, in 2004 Cohen et al. [34] proposed an FGFET device for in *vitro* application consisting of a p-type transistor with an insulated poly-silicon gate (covered by 420 Å of thermally growth oxide) that acted as the recording site.

3 Equivalent Circuit: Impedance parameter extraction

Abstract

This chapter provides a methodology to evaluate the performance of a sensing electrode to measure electrophysiological signals *in vitro*. The methodology relies on a description of the sensing interface by an equivalent circuit. Each circuit component is related with a physical parameter that controls the electrical coupling of the signal to the sensing surface. The extraction of the individual circuit parameters is carried-out by using three types of measurements (a) small-signal impedance measurements, (b) circuit transient response and (c) by quasi-static methods. The extraction of this circuit parameters can be used to select the best materials for sensing electrodes and/or to optimize the electrode design.

3.1 Introduction

In the previous chapter we lay down the basic equivalent circuit that describes the sensing interface. The role of each individual circuit component in controlling the signal quality and the signal shape was described. Electrodes fabricated using different materials will show a different performance that is related with the way they establish an interfacial double-layer with the electrolyte solution. Having methodologies to extract the circuit elements that characterize the interface is important because it allows the experimentalist to quantitatively evaluate materials for bioelectrical signal transduction.

This chapter describes the methodology to fully characterize a sensing electrode. This methodology makes use of the measurement of the small-signal impedance as well as the transient response of the electrodes.

3.2 Parameter extraction

In Chapter 2 we presented the equivalent circuit that describes how a bioelectrical signal is coupled to a sensing electrode. The circuit can be simplified to the circuit showed in Fig. 6 Basically, this circuit only takes into account the double-layer capacitance (C_D), the double-layer resistance (R_D) and the spread resistance (R_C). In order to extract this individual circuit components three different methodologies are required, (a) small-signal-impedance measurements and (b) transient response, and (c) quasi-static methods. In the following sections we explain these methods.

(a) Small-signal impedance measurements

To extract C_D and R_D we can measure the small-signal impedance. Basically, we connect an impedance analyzer to the electrode system and measure the frequency response of the impedance.

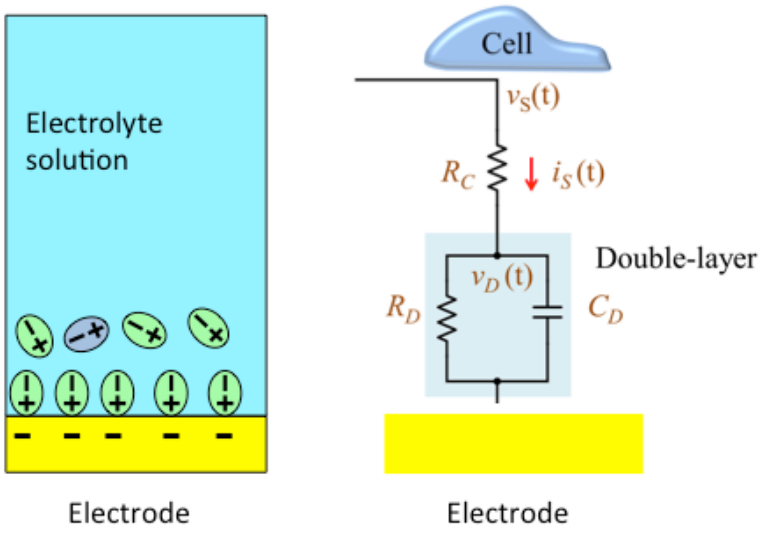

Fig. 6: Equivalent circuit that describes the electrode/solution interface region.

Typically, electrode/electrolyte systems behave as a two-layer system, with one interfacial layer having a high capacitance (electrical double-layer) in series with a low capacitance layer (bulk electrolyte). This two-layer system is described as a series sum of two parallel RC networks as shown in the inset of Fig. 7. The two RC circuits are a way to describe the two-layer system, we do not have access to each individual circuit. When an impedance analyzer is connected to the electrodes what is measured is a frequency-dependent parallel resistor (R_P) and a capacitor (C_P). We can only extract the individual circuit parameters by fitting the experimental values of R_P and C_P with the double RC network.

At low frequencies, the high capacitive interfacial layer is probed. As the frequency increases the high capacitance is short-circuited giving rise to a transition from a high capacitance to a low capacitance that corresponds to the series sum of the interfacial and bulk capacitance. This is known as a Maxwell-Wagner relaxation. In general metallic electrodes such as gold immersed in electrolyte solutions exhibit this behavior. In the terminology explained in chapter 2, these electrodes are known as polarized electrodes or Faradic electrodes.

The series of the two RC networks will have an overall equivalent resistance (R_P) and capacitance (C_P) that are measured externally using an impedance analyzer.

The equivalent admittance Y_T of the series-parallel network is given by

$$Y_T = \frac{1}{R_P} + j\omega C_P \quad (1)$$

Where R_P and C_P are the total parallel resistance and capacitance, respectively, given by

$$C_P(\omega) = \frac{R_D^2 C_D + R_S^2 C_S + \omega^2 R_D^2 R_S^2 C_D C_S (C_D + C_S)}{(R_D + R_S)^2 + \omega^2 R_D^2 R_S^2 (C_D + C_S)^2} \quad (2)$$

$$R_P(\omega) = \frac{(R_D + R_S)^2 + \omega^2 R_D^2 R_S^2 (C_D + C_S)^2}{R_D + R_S + \omega^2 R_S R_D (R_D C_D^2 + R_S C_D^2)} \quad (3)$$

Fig. 7 shows also the capacitance (C_P) and the Loss ($1/(\omega R_P)$) curves for an Au electrode. The curves were fitted to the response predicted by the equivalent circuit shown on the inset of Fig. 7 Fitting parameters are presented in Fig. 7 caption. The impedance of this two-layer system has a relaxation near 3 kHz know as Maxwell-Wagner relaxation. The fitting is not perfect because the low frequency dispersion has not been taken into account in our model. Usually, a constant phase element must be added to the equivalent circuit network to fit the dispersion at low frequencies.

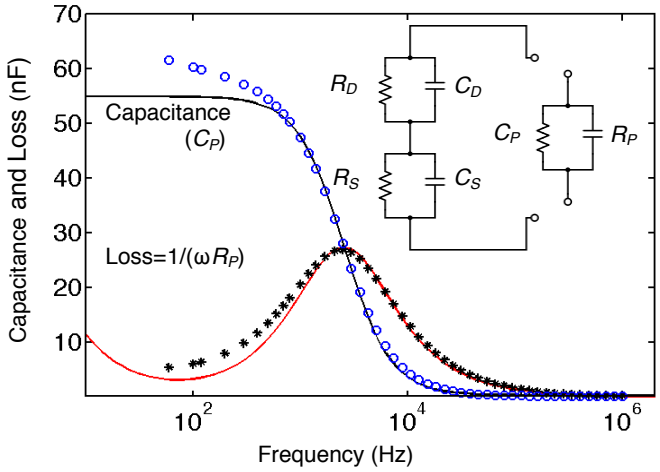

Fig. 7: Typical frequency dependence of a gold electrode system immersed in a cell culture medium. The capacitance and loss as function of the frequency has a dispersion know as Maxwell-Wagner relaxation. The inset shows the equivalent circuit used to fit the experimental data (thick lines). Fitting parameters are R_D =1.4 MΩ, C_D =55 nF, R_S =1.13 kΩ, C_S =0.36 nF. The data is relative to a gold electrode immersed in a cell culture medium.

Fig. 8 compares the frequency dependence of a gold electrode (Fig. 8(a)) with a polymer electrode (Fig. 8 (b)) under identical conditions. For both materials the capacitance and loss are frequency dependent. However, in contrast with the gold, the polymer-based electrode shows a loss that rises rapidly for low frequencies. This shows that the interface has a very low resistance when compared with gold. The bulk electrolyte resistance (R_S) is estimated to be approximately 1.3 kΩ while the interfacial double-layer resistance (R_D) is estimated to be around 300 Ω. Interesting, the polymer/electrolyte system does not behave as a two-layer system and therefore does not show a Maxwell-Wagner relaxation as observed for the gold/electrolyte system.

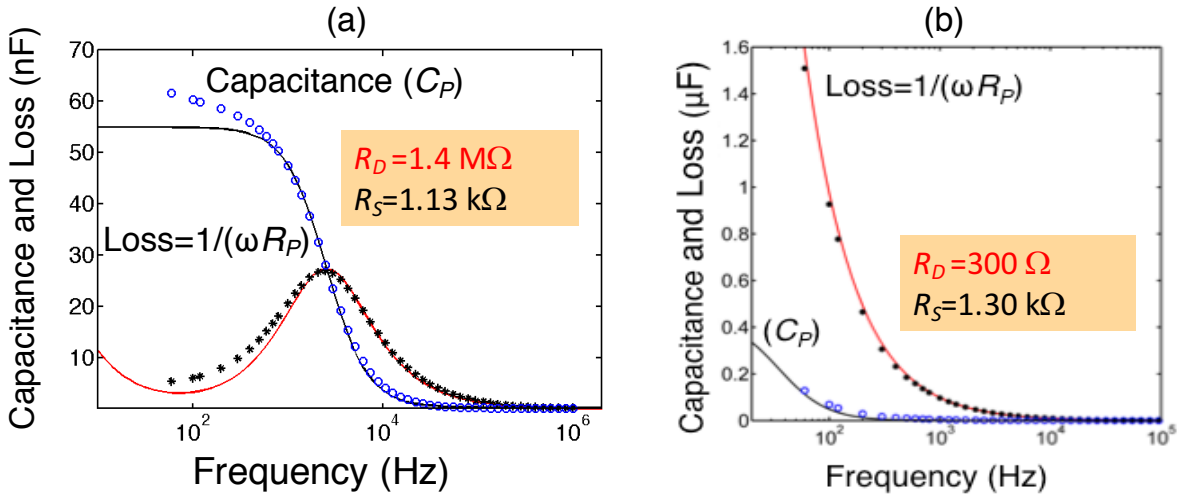

Fig. 8: Comparison between the impedance of a gold electrode system with a printed PEDOT:PSS electrode. (a) Gold electrode, and (b) PEDOT:PSS electrode. Fitting parameters for the polymer based system are R_D=300 Ω, C_D=55 nF, R_S=1.3 kΩ, C_S=0.36 nF.

Fig. 9 compares the plots of capacitance and the loss for the gold/electrolyte and for the polymer/electrolyte interfaces. This representation helps to elucidate further the major differences between the two electrode systems. In the frequency range above 100 Hz the interfacial capacitance of the gold is higher than the capacitance of the polymer. However, the extrapolation of the polymer capacitance to very low frequencies (dashed line in Fig. 9 (a).) suggests that for very low frequencies (not accessible with our impedance analyzer, Fluke RCL meter PM6306) the polymer capacitance will overtake the gold capacitance. The comparison of the loss curve in Fig. 9 (b) shows that the polymer/electrolyte interface is significantly more conductive than a gold/electrolyte interface.

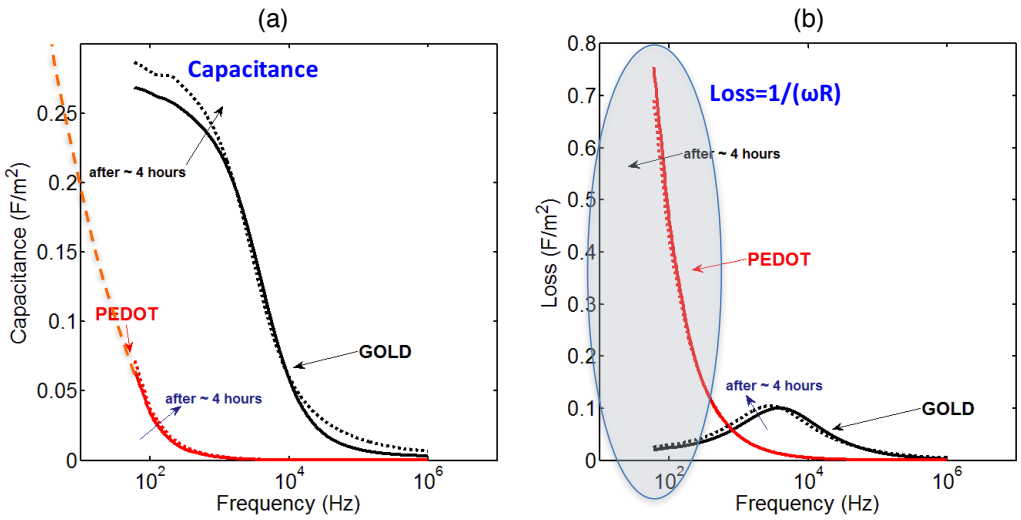

Fig. 9: Comparison of the impedance parameters of a gold and a polymer electrode system. (a) Comparison of a capacitance and (b) the loss for the gold and polymer system.

(b) transient response

In our measurement setup we use a trans-impedance amplifier, whose output voltage is given by

$$v_o(t) = -R_F i_S(t) \qquad (1)$$

where R_F is the feedback resistance and $i_S(t)$ the current flowing trough the measuring electrode impedance. It is important to understand how this current is related with v_S (t), the voltage signal generated by the cell. Fig. 10 shows the circuit used to derive the relation between $v_S(t)$ and $i_S(t)$. As discussed above we assume that Z_{Seal} is high and the cell generated current signal $i_{SC}(t)$ is effectively coupled into the measuring electrode ($i_{SC} \approx i_S$).

First we express $i_S(t)$ in function of $v_C(t)$, the voltage across the double-layer capacitor,

$$i_S(t) = \frac{v_C(t)}{R_D} + C_D \frac{dv_C(t)}{dt} \qquad (2)$$

The (-) input of the amplifier is a virtual ground and therefore,

$$v_S(t) = \left(\frac{v_C(t)}{R_D} + C_D \frac{dv_C(t)}{dt}\right) R_C + v_C(t) \qquad (3)$$

This equation can be rearranged as:

$$\frac{dv_C(t)}{dt} + \frac{(R_D + R_C)v_C(t)}{R_D R_C C_D} = \frac{v_S(t)}{R_C C_D} \qquad (4)$$

Considering a particular solution of (4), when $v_S(t)$ is a voltage ramp rising at constant rate m i.e. $m=dv_S(t)/dt$, then the solution of equation (4) yields:

$$v_C(t) = k\left[t - \tau\left(1 - e^{-t/\tau}\right)\right] \tag{5}$$

where

$$k = \frac{R_D m}{R_D + R_C} \tag{6}$$

and

$$\tau = \frac{R_D R_C C_D}{R_D + R_C} = C_D(R_C // R_D) \tag{7}$$

τ is the time constant for the device to be charged or discharged. The electrical current, $i_S(t)$, through the circuit can now be readily calculated by replacing (5) into (2) as:

$$i_S(t) = \frac{kt}{R_D} + \frac{k\tau}{R_C}\left(1 - e^{-t/\tau}\right) \tag{8}$$

Since $R_D \gg R_C$, the time constant for the device is $\tau \cong R_C C_D$. In this limit the current is given by

$$i_S(t) \cong \frac{mt}{R_D} + mC_D(1 - e^{-t/\tau}) \tag{9}$$

$i_S(t)$ signal is the sum of two independent terms, a component proportional to $v_S(t) = mt$ and a transient term with a peak amplitude proportional to the product mC_D that decays with a time constant $\tau \cong R_C C_D$.

Hence, C_D acts as a multiplying factor for the current. Basically, a rapidly varying voltage signal (with a large *m)* produces a large transient displacement current across the capacitor. Under these conditions, the measured current signal shape is also proportional to *m*, the derivative of the original signal $v_s(t)$.

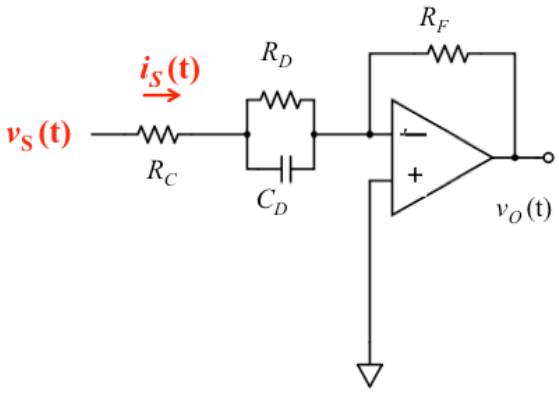

Fig. 10: Equivalent circuit together with the trans-impedance amplifier i_S (t) is the signal generated by the cell.

To understand how the signal shape is affected by the circuit components let us simulate the current response as predicted by Eq. (9) to a square voltage pulse. The simulation is represented in Fig. 11 . As expected at the rising and falling edges of the voltage pulse the time derivative, dv_S/dt, forces a large surge current through the capacitor giving rise to a upward and to a downward current spike. The current spike should fall down to zero when R_D is large and to a constant DC value when R_D is small.

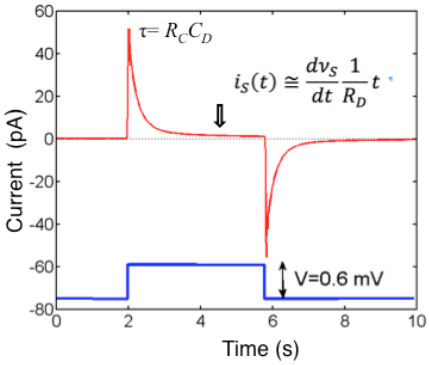

Fig. 11: Relation between the equivalent circuit parameters and the signal shape when measured in current.

The value of R_D has an important role on the signal shape. If R_D is large the signal in current is just comprises of spikes. However if R_D is small the leakage current will increase and will modify the signal shape. The signal shape will approach to a square signal if R_D is small. Fig. 12 shows an example how the signal shape changes as the Value of R_D changes. The changes in R_D were introduced by using different electrodes and substrates.

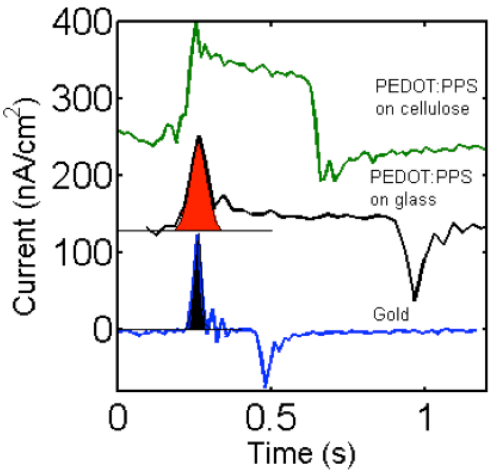

Fig. 12: How the signal shape in current changes when R_D decreases. Using different electrode materials and different substrates brought the variation in R_D.

(c) quasi-static methods.

In general the impedance of the electrode/electrolyte systems is strongly frequency dependent. Small-signal impedance techniques are limited to a few Hertz. For comparison purposes it may be desirable to measure the quasi-static capacitance (QS-C). The QS-C is estimated from the equation of $Q=CV$ or $C=I/(dv/dt)$, and it requires linear ramp rate or voltage. For more reliable capacitance estimation the voltage ramp is varied and the corresponding displacement current measured. The plot of the voltage ramp rate *versus* the displacement current gives a straight line. From the slope one can extract the capacitance. Fig. 13 shows an example of this method applied to one of our devices.

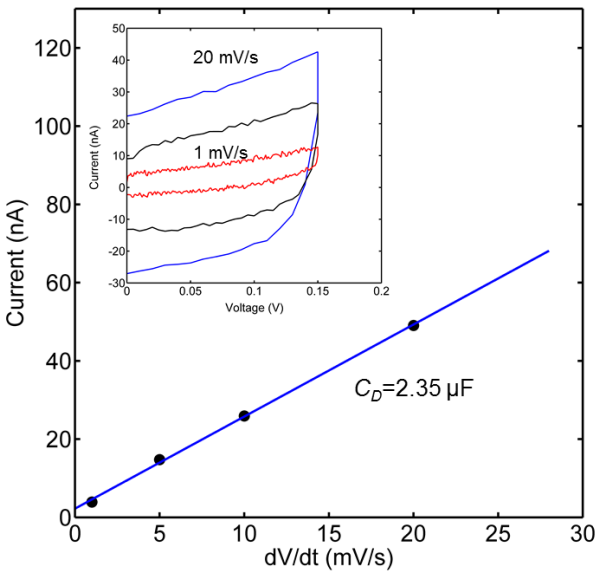

Fig. 13: Method to estimate the quasi-static capacitance. Plot of the displacement current versus voltage ramp rate. The inset shows the current-voltage (*I-V*) hysteresis loops from each of the displacement current estimated.

3.3 Conclusions

This chapter presents a methodology to extract the equivalent circuit parameters, which describe the electrical coupling of a signal to a sensing electrode. This quantitative information can be used to optimize the electrode geometry, and also to select the best materials for electrophysiological applications.

4 Electrical characterization of mushroom-shaped gold microelectrodes

Abstract

In this chapter mushroom-shaped microelectrodes are electrically characterized using small-signal impedance techniques, current voltage measurements and transient response to a voltage pulse. The enhancement of the capacitance caused by the mushroom micro structured surface is compared with the bare flat gold surface. Two types of mushrooms were electrically characterized, gold and polymer based mushrooms.

4.1 Introduction

Increasing the area of the electrodes causes an increase in sensitivity due to the reduction in noise and impedance. However, as the area increases the ability to discriminate between individual cell signals is impaired. To circumvent this trade-off between electrode sensitivity and spatial resolution several laboratories have started to develop structured electrodes. These emergent electrodes make use of vertical micro or nano-structures[35], [36] coated, namely, with carbon nanotubes,[37]–[39], or conducting polymers[17], [40]–[48], which provide a softer and more roughened surface. The strategy behind these approaches is to increase the effective area and to promote a more intimate interaction of the electrode with cells. A well-known example is the use of micron size gold mushroom-like shapes[49], [50]. It has been shown that cells engulf the protruding gold mushroom-like shapes, lowering the impedance and improving the electrical coupling between the cells and the electrode.

This chapter presents an electrical characterization study of a gold surface coated with an array of micro-mushroom like shapes. These electrodes are fabricated by the University of Porto Physics Department and supplied to us.

The chapter starts by briefly presenting how these electrodes are fabricated. Scanning electron photographs (SEM) are shown to provide a view of the micro-mushroom morphology. This is followed by a description of the experimental set-up developed by us to perform electrical measurements. Namely, we show the chip holder developed to contain the cell culture medium and the reference electrode. The electrodes are electrically characterized using impedance methods and transient techniques.

4.2 Fabrication of mushroom-shaped microelectrodes

The fabrication starts by using a flat gold surface coated in a photosensitive polymer (photo resist) deposited by spin coating. This photoresist polymer surface is exposed to a laser direct write system to write a pattern. The pattern is constituted by an array of circles with 2 µm and 1.5 µm of diameter and a pitch of 10 µm. The total area of the pattern is 4 mm^2. The pattern layout is made in AutoCAD and physically imprinted by the laser into the polymer surface.

In the regions where the polymer was exposed to the laser light, the polymer chemical bond connections are destroyed. If this substrate is then washed with a solvent the damage polymer is removed and leaves a pattern of micro-pores on the polymer surface. This technique

is very similar to conventional photolithography used in the semiconductor industry. However, the patterns are not made by using a mask but by a laser.

The pattern surface of micro-pores is then immersed into a solution with gold particles (Orosene solution). Upon the application of well-defined potentials, gold is electrodeposited through the micro-pores on the underneath gold surface. With time the gold fills the micro-pores. However, as it reaches the polymer surface the gold is no longer confined by the pore dimensions and grows sideways on the polymer surface creating the mushroom cap. The size and shape of this top cap is then determined by the electrodepositing parameters used. Fig. 15, Fig. 16 and Fig. 17 shows some Scanning electron micrographs with a variety of mushroom shapes. These shapes are controlled by the electrodeposition parameters.

All the parameters to optimize the morphology and geometry have been optimized by the University of Porto. For further details the reader is recommend to read the Msc. thesis of Monica Cerquido [51].

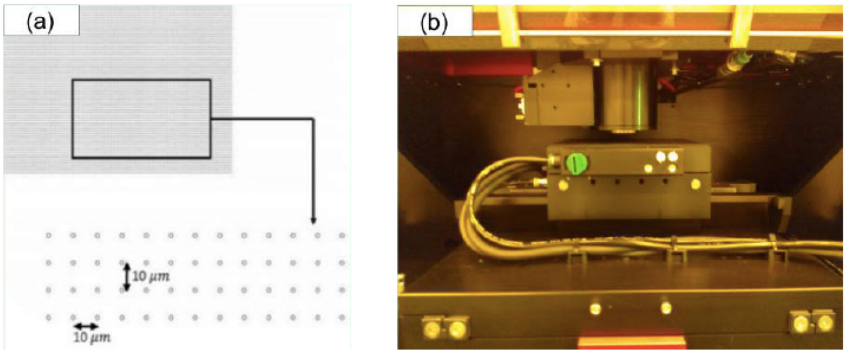

Fig. 14: Pattern and the Laser direct write system. (a) Pattern designed in AutoCad and (b) Photograph of the optical lithography system.

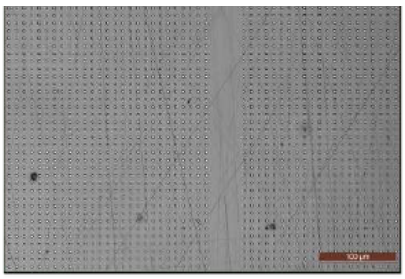

Fig. 15: Optical microscope image of the transferred patterns produced in a photoresist.

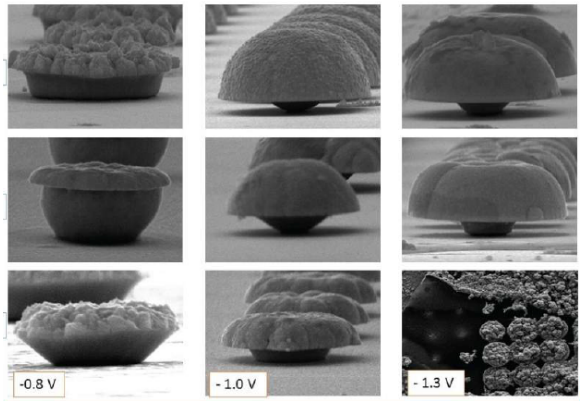

Fig. 16: SEM micrographs of the gold-mushrooms microelectrodes plated at different electrodepositing potentials.

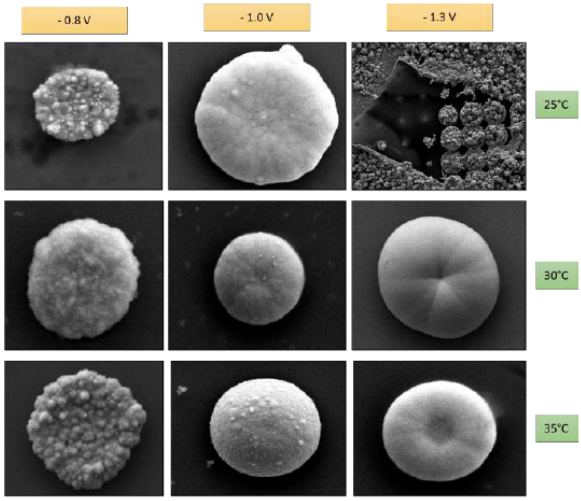

Fig. 17: Top view of the produced gold-mushroom microelectrode using different temperatures and potentials.

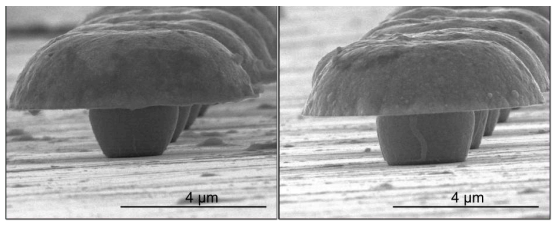

Fig. 18: SEM images of the microelectrodes produced by two different pixel pulse durations.

The basic structure of the sensing device together with the electrical connections and the cells is represented in Fig. 19. A schematic diagram of the gold mushroom-shaped electrode and the electrical connections to the voltage amplifier is represented in Fig. 19(a). Fig. 19(b) shows a scanning electron microscopy photograph of the gold mushroom structured surface. The mushroom density is 4753 mushrooms per mm^2. A schematic diagram of the integration

of the sensing electrode in an acrylic vessel is schematically represented in Fig. 19(c) and a photograph of a real device is shown in Fig. 19(d).

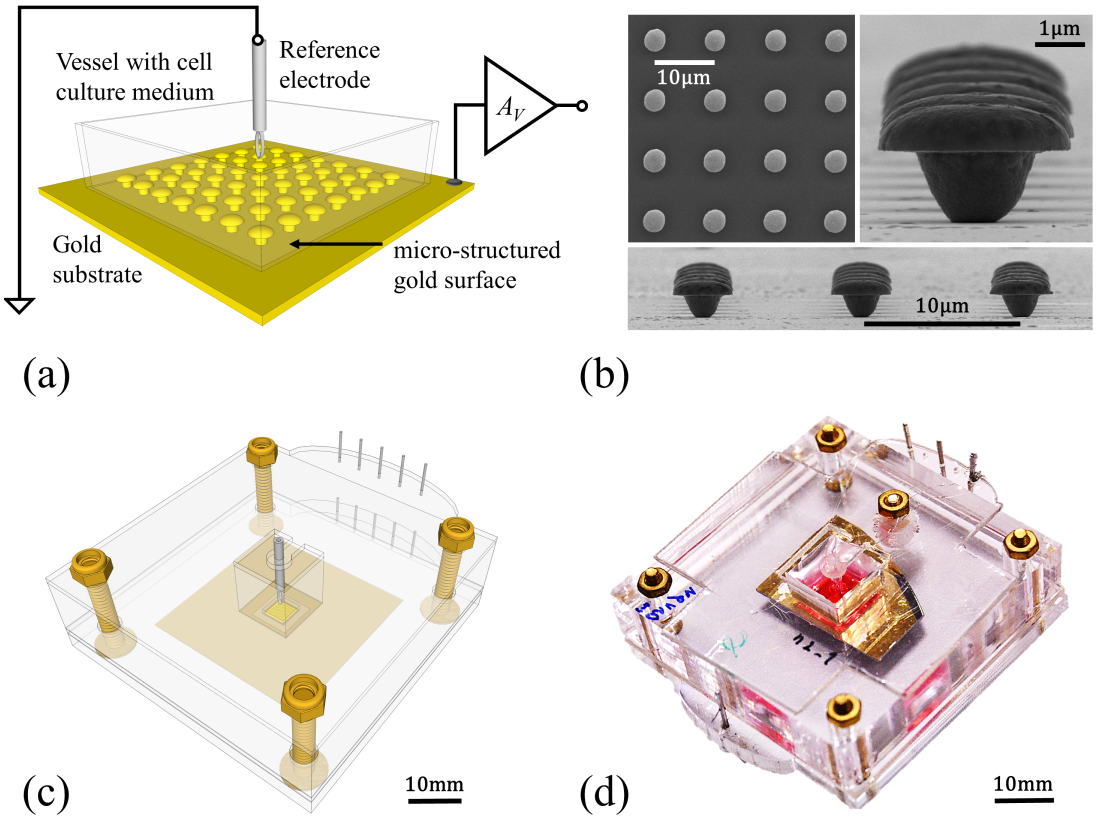

Fig. 19: (a) Schematic diagram of the device and electrical connections. (b) Scanning electron microscopy (SEM) photographs of the gold mushroom structures, (c) top view and (d) Photograph of the chip holder with the device ready for measurements. The SEM photographs are from Msc thesis by Mónica Crequido [51].

4.3 Results

4.3.1 Electrical Impedance

Measurements of the electrode impedance and electrical noise were first carried out to provide insight into the sensitivity of the electrodes and the advantages of using a micro-structured surface in comparison with a flat gold electrode.

The small-signal impedance between the mushroom shaped electrode and the AgCl coated wire was measured in the frequency range from 50 Hz to 1MHz. The frequency dependence of the capacitance (C) and the loss $\left(\frac{1}{R\omega}\right)$ is shown in Fig. 20. The impedance has a typical Maxwell-Wagner relaxation centered between 3 to 4 kHz. The sensing electrode has an area of 0.0625 cm^2 and low frequency capacitance is approximately 200 nF. This corresponds to a low-frequency capacitance per unit area of 3.2 $\mu F/cm^2$.

The impedance drifts slowly with time. The capacitance decreases and the resistance increases with time.

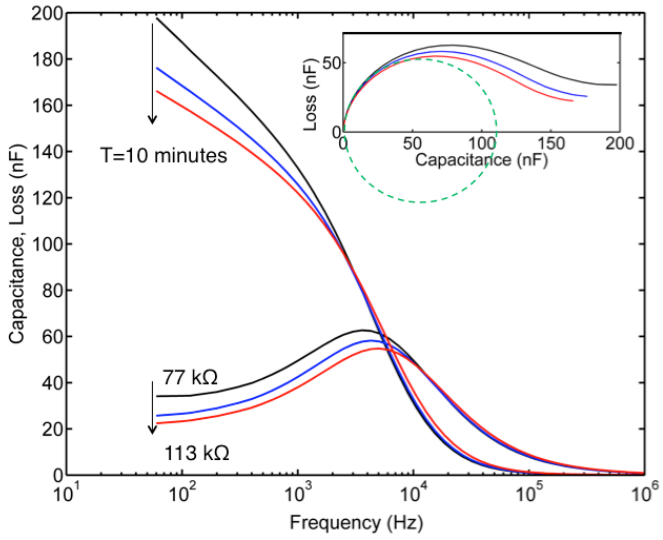

Fig. 20: The frequency dependence of the capacitance and loss. The inset shows the same data represented in a Cole-Cole plot. An ideal Maxwell-Wagner relaxation should give a perfect semicircle center on the XX axis as the green semicircle in the figure suggests.

The power spectral density of the voltage noise, S_V, as a function of frequency is shown in Fig. 21(a). We use 10 time series to obtain the averaged noise. The dashed lines represent the power-law behavior for reference. The magnitude of the noise decreases with the frequency, and for frequencies higher than 1 kHz the noise becomes frequency independent. For frequencies below 100 Hz, the noise follows a $1/f$ law that evolves for the lowest frequencies to a $1/f^2$ frequency dependency (flicker noise). This frequency dependence is typical of electrodes in electrolyte systems. The $1/f$ power law agrees with the frequency dependence of the system total resistance, R_P, (see Fig. 21 (b)) confirming that the intrinsic thermal noise of the resistive elements dominates the electrical noise of the recording system. The inset in Fig. 21 (a) shows a short time trace of the noise measured in the frequency band of 0.1 to 12.5 Hz. The voltage noise is 0.3 μV peak-to-peak and determines the detection limit of our measuring system for signals in the frequency range of a 0.1-12.5 Hz.

In Fig. 21 (c) we present a comparison of the frequency response of the individual impedance parameters capacitance (C_P) and resistance (R_P) of a bare flat gold electrode with a mushroom covered surface. For convenience, the resistance (R_P) is represented as Loss (L_P=1/(ωR_P)). Both C_P and L_P are strongly frequency dependent. This frequency dependence of the impedance has been extensively studied by us[52] and others[53] and was shown to be characterized by a Maxwell-Wagner dispersion, typical of electrodes immersed in electrolyte solutions. Fig. 21 (c) this dispersion is located at 10 kHz and corresponds to the frequency position of the peak in the Loss curve. The dispersion occurs because electrodes immersed in electrolyte solutions give rise to electrochemical double-layers with high capacitances (C_D) and high resistances (R_D). This interface layer appears in series with the rest of the electrolyte solution. When compared with the double-layer, the bulk region has a lower capacitance (C_B) as well as lower bulk resistance (R_B). At low frequencies the high capacitance layer dominates, however, and as the frequency increases the interfacial layer is progressively short-circuited and the low capacitive bulk layer starts to dominate the system response. The transition in frequency between the two layers is responsible for two capacitance plateaus shown in Fig. 21 (c), one at low and the other at high frequencies. The values of C_P and L_P below the loss peak are related with the interfacial or double-layer region and the values above the relaxation peak are related with the bulk electrolyte solution. The relaxation frequency is mostly controlled by the bulk electrolyte resistance, RB [52]. Both flat and micro-structured gold electrode were immersed in the same electrolyte solution, and therefore, as expected, the relaxation frequency must have the same value for both systems, as confirmed by the data in Fig. 21 (c). The

difference between the two electrodes is the surface topology; one surface is micro-structured and the other is flat. At 100 Hz the micro-structured surface has a capacitance 30 nF higher than the flat surface. The corresponding double-layer resistance is also lower by 23 kΩ.

As shown in Fig. 21 (c), both C_P and L_P do not reach steady state values at 100 Hz. Instead, they follow a trend to increasing values for lower frequencies. It is expected that the quasi-static capacitance (for f=0Hz) is significantly higher than the values measured at 100 Hz. The quasi-static values for C_D were obtained by measuring the displacement current $i_D(t)$ in response to a slow voltage ramp dv/dt. The inset of Fig. 21 (c) shows the displacement current for flat and micro-structured surfaces. The quasi-static capacitance (Csta) is estimated to be 0.6 μF for flat gold electrode and 1.1 μF for the micro-structured gold electrode. This represents an increase of about 54 % in the quasi-static capacitance.

As discussed above the higher the capacitance the higher the electrical coupling of the signal to the electrode. Previously, we have reported that in voltage detection methods, the SNR increases linearly with the capacitance[54]. Therefore, assuming that the number of cells synchronized is constant, we would expect an increase in 54% in the SNR in comparison with a flat gold surface.

The slope of the straight lines on the inset of Fig. 21 (c) provides the quasi-static capacitance. The obtained values are 0.64 μF for the flat gold surface and 1.1 μF for the mushroom surface. Therefore, the nanostructured polymer surface has an interfacial capacitance that is 1.8 times larger than the flat gold surface.

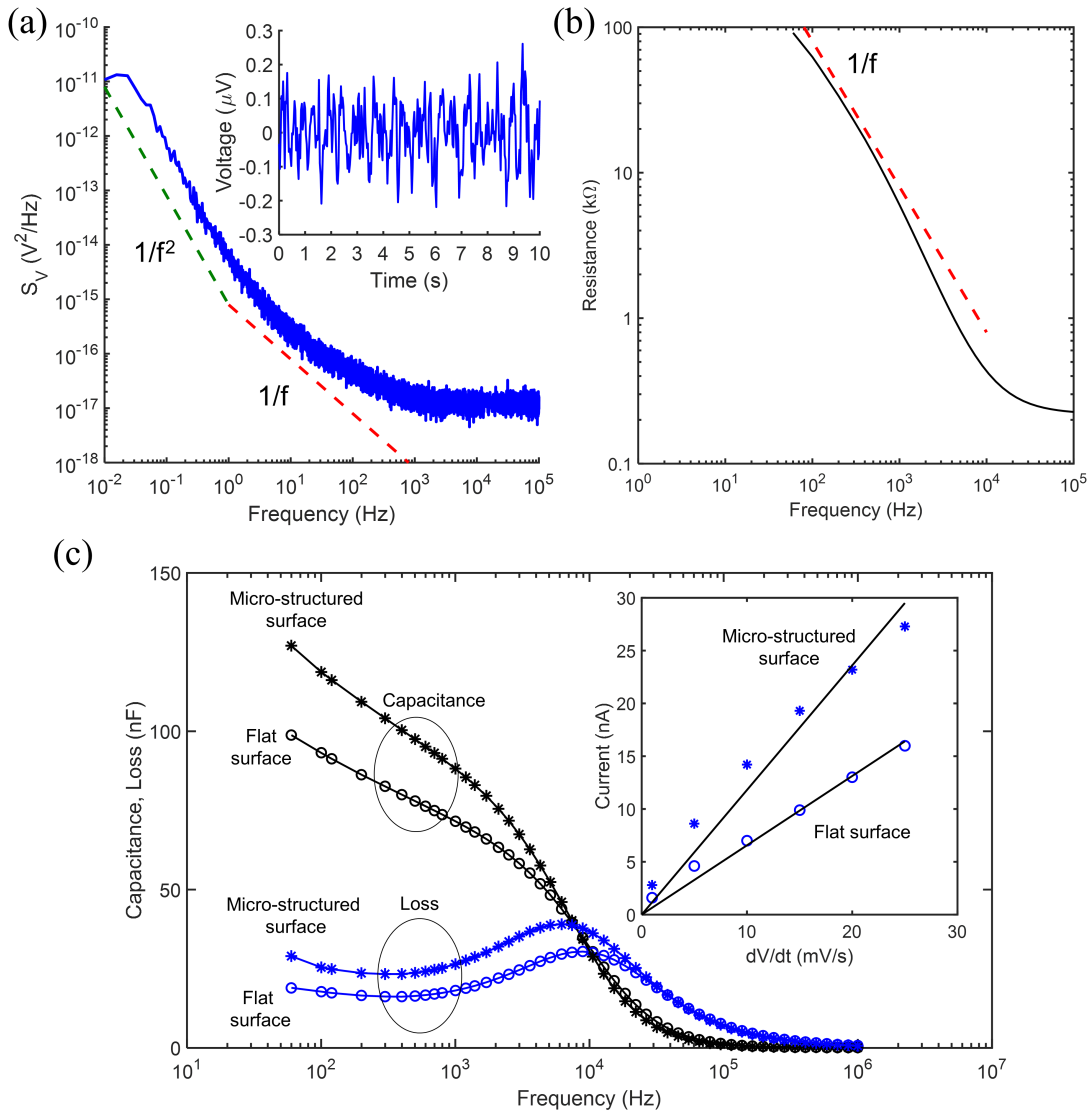

Fig. 21: Electrical properties of the sensing electrodes. (a) Frequency dependence of the noise power density in voltage, inset: Noise. (b) Frequency dependence of the total system resistance, RP. S_V was measured by dividing the full frequency range (105 Hz) in several shorter ranges. The total smoothed power spectrum was obtained by joining the frequency segments. (c) Frequency dependence of the impedance components, capacitance (*CP*) and Loss *(LP=1/(ωRP))*. The inset compares the displacement current measured for a micro-structured and for a flat electrode.

4.3.2 Transient response

In this section we compare the transient response of a polymer mushroom coated surface with the flat gold surface. The objective is to extract the device parameters as explained in Chapter 2. Fig. 22 shows the response to a voltage step of 2 mV. The response can be well described by an exponential as show in the inset of Fig. 22. The flat gold surface shows a decay time of τ_{gold} = 36.6 µs whereas the mushroom polymer surface has a decay time of $\tau_{polymer}$ = 38.3 µs. τ was calculated from the slope of semi log plot, inset on the Fig. 22.

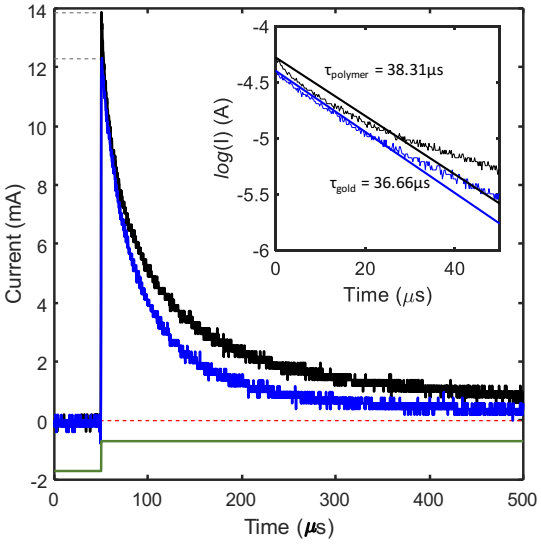

Fig. 22: Transient response to the application of a voltage step 2 mV. The inset compares the decay time for a flat gold surface and for polymer based mushroom surface.

The spreading resistance $R_{C,}$ can now be estimated from the following equation

$$R_C = \frac{\tau}{C_{DS}}$$

where τ was estimated from the transient response to a voltage step and C_{DS} is the quasi-static depletion capacitance. C_{DS} is estimated form the displacement current (see Fig. 21). Replacing the parameters obtained for both systems, we obtain for the spreading resistance of the polymer/electrolyte interface, $R_{CPolymer}$=26.4 Ω and for the spreading resistance of the flat gold/electrolyte interfacial region we obtain R_{CGold}=114.3 Ω. Interesting the polymer mushroom surface provides a lower spreading resistance and therefore a lower signal loss.

4.3.3 Abnormal transient response to a train of voltage pulses

When a train of pulses is applied to the mushrooms the system responds with an abnormal transient response. Fig. 23 shows the voltage response after the application of a train of pulses (amplitude of 20 mV, duration 5 ms, and 25% duty cycle). The total duration of the voltage train is 1 minute.

Immediately, after the voltage train is applied, the voltage of the electrode goes to a very low negative voltage value (millivolts). The initial negative peak value of the voltage transient is not recorded because it saturates the amplifier. The high negative voltage decays rapidly. In 25 seconds the voltage decay cross the baseline (V=0). Interesting, after passing through the baseline the voltage reverts its polarity and increases to a positive peak value of approximately 85 μV. Then this positive voltage fluctuation decays slowly to the base line potential. The inset in Fig. 22 shows the voltage decay represented in a semi-logarithmic plot. The estimated time constant τ, is 59.2 s.

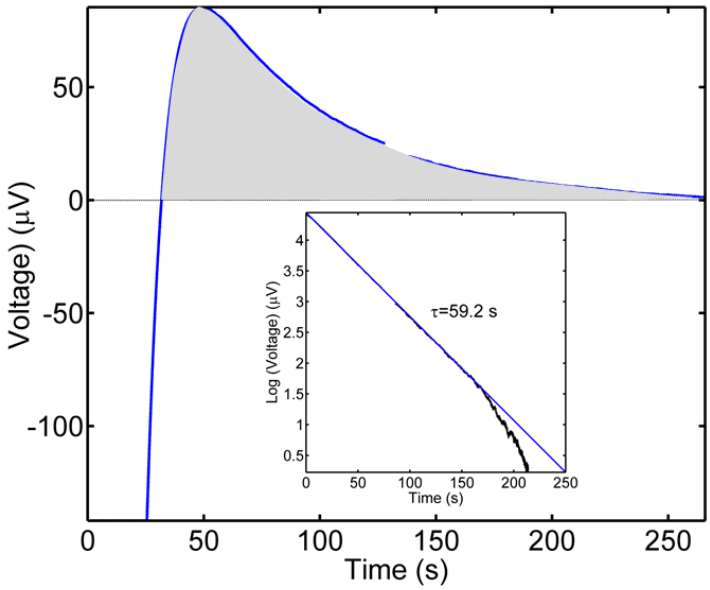

Fig. 23: Transient voltage response upon the application of a train of voltage pulses.

The filled area under the curve shows the positive part of the oscillation after the voltage train is applied.

The transient response shown in Fig. 23 is abnormal because it has two distinct voltage oscillations. First a negative component that decays rapidly and cross the baseline. The total transient shape shown in Fig. 23 suggest that there is a charge inversion process at the

electrode/electrolyte interface. First, when it is submitted to an external driving voltage the electrode/electrolyte interface polarizes with a negative charge. Once the external applied voltage is released, the negative cloud does not disappear instantaneously because it is comprised of slow moving negative ionic species. This unbalance negative charge will attract the positive ionic species from the surrounding solution. For some reason not clear yet, the final result of this electrostatic interaction between ionic species at the interface is a net positive charge. This net positive charge decays exponential with time as shown in Fig. 23.

This transient response resembles to a strongly damped oscillating behavior and in principle should be described by an equivalent RCL circuit. However, the inductor element in this case does not have a physical meaning.

In a separate experiment a set of short voltage trains separated by approximately 10 minutes were applied. In between voltage trains, the corresponding voltage transient is recorded. The behavior for an ensemble of voltage trains with duration of only 20s is show in Fig. 24. The positive voltage peak corresponds to the excess positive charged oscillation describe above. Upon the successive application of identical voltage trains the peak value of the positive voltage oscillation keeps increasing with time, until eventually saturates. Even with 10 minutes of interval between voltage trains the system remembers how many pulses have been applied. The system has memory (in a time scale of minutes). The physical origin of this memory effect in a time scale of several minutes is still unknown.

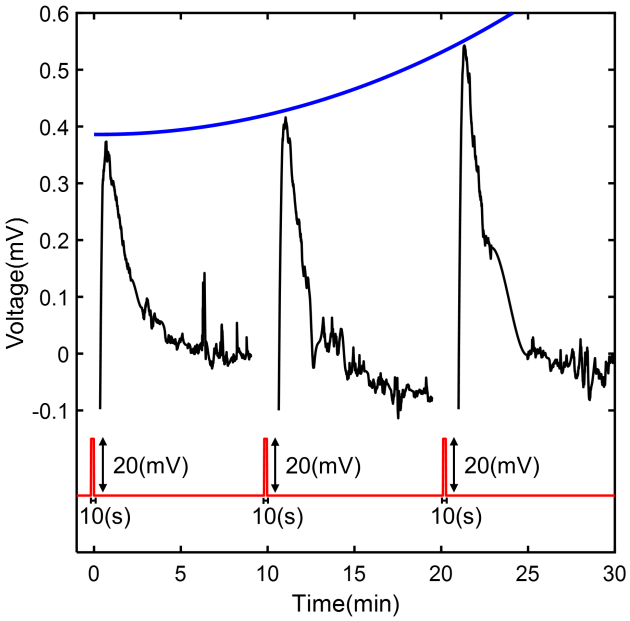

Fig. 24: The effect of the application of 3 successive voltage trains separated apart by approximately 10 minutes. Although the abnormal positive voltage fluctuation has enough time to relax to the base

line, the system still remembers how may pulses have been applied before. Each individual voltage train has duration of 10 s, amplitude of 20 mV, pulse duration of 5 ms and a duty cycle of 25%. The amplitude of the positive oscillation will reach a peak where it saturates.

4.4 Discussion and conclusions

The procedure to extract the equivalent circuit described in Chapter 2 was applied here to in a quantitative way compare the differences between a flat gold surface and a polymer mushroom surface. It was demonstrated that the micro-structured polymer surface enhances the electrode/electrolyte interfacial capacitance and lowers the interfacial resistance. From the transient response we extract the spreading resistance (R_C) for both interfaces. As expected the spreading resistance is low. Furthermore, the polymer/electrolyte interface shows an even lower spreading resistance. Low spreading resistances are essential to have a good electrical coupling of the bioelectrical signal to the sensing electrode.

The response of our devices to a voltage step follows a textbook behavior with an exponential decay with time. However, when several pulses are consecutively applied to the electrode/electrolyte interface the transient response becomes non-linear. After the application of a long train of voltage pulses the voltage transient is comprised of two components of opposite charges. We tentatively explained this non-linear response as a complex interaction of unbalance ionic species at the electrode/electrolyte interface. This ionic interaction also develops a kind of memory effect on a time scale of few minutes. Physical explanation for this memory effect is still lacking.

5 Electrical stimulation of glioma cells populations using mushroom-shaped gold microelectrodes

Abstract

Mushroom-shaped gold microelectrodes were used to electrical stimulate a population of Rat glioma C6 cells. The application of a train of voltage pulses triggers quasi-periodic oscillations with an average period of 42s. Signal shapes are biphasic.

5.1 Experimental

Electrical stimulation was performed using a train of voltage pulses with a frequency of 0.5 Hz, with 20 mV in amplitude, 100 microseconds width and a rise time of 20ns. The pulses were applied to the glioma cell culture for a period of 1 minute. The experimental setups described in Fig. 25.

Rat glioma C6 cells (American Type Culture Collection, ATCC) were cultured in 15% F-12K nutrient mixture supplemented with 15% of fetal horse serum, 2.5% of fetal bovine serum and 1% of penicillin and streptomycin. The cells were maintained at 37 ºC in an incubator with a humidified atmosphere with 5% of CO_2. The cells were harvested from the culture plates and diluted in culture medium to yield cell suspensions with a known cell density and transferred to the sensing devices. An aliquot of 350 µL of the cell suspension with a concentration of $5.1x10^6$ cells/mL was transferred to the well of the transducer and cells were allowed to sediment onto the electrodes for 2h before any measurements were performed. Prior to cell deposition the transducers were sterilized by UV treatment and the electrodes were coated with poly-L-lysine to promote cell adhesion. UV sterilization was accomplished by using a Bio air device with a Sankyo Denki G30T8 lamp with UV-C in the range of 200-280 nm. Time under UV light was about 30 minutes. The transducer was placed 20 cm away from the lamp.

Cell viability and pH kinetics essay's were performed both in the transducer as well as in 96 well plates. $4x10^5$ cells were seeded in 350 µl culture medium, with cell-free wells as controls. The pH on supernatants was measured with Lab850 pH-meter (Schott Instruments). Cell numbers and viability was assessed using a Neubauer chamber-based trypan blue live/dead exclusion assay.

Cells are equally viable in the transducer and in 96 well plates. Cell number assays show identical values for both substrates.

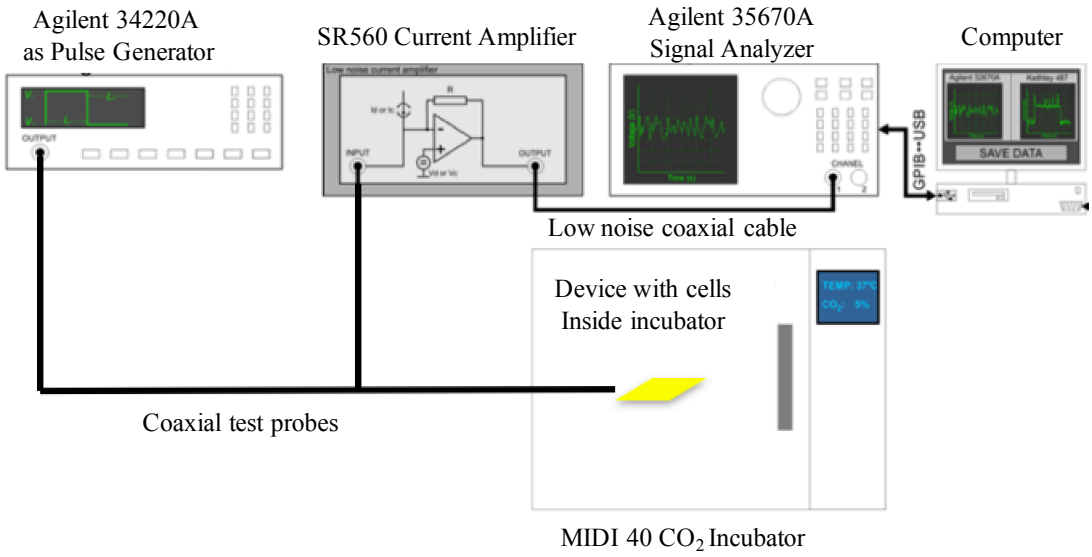

Fig. 25: Our experimental setup, used to stimulate the cells, and measure the outcoming signals.

5.2 Results

5.2.1 Electrical stimulation

Electrical stimulation was performed using a train of voltage pulses applied to the gold sensing electrode as described in the introduction. Fig. 26 shows the transient response of the device coated with a population of glioma cells (200.000 cells). The transient response (after the pulse is removed) is characterized by a fast decay followed by an overshooting process. The settling time to baseline last approximately 5-6 minutes.

Simple RC networks often used to describe the transient response of an electrochemical double-layer to a voltage cannot predict the overshooting process observed. After overshooting and during the settling time, 3 signals are observed. These signals are separated in time by 40 seconds with a typical width of 10 seconds, they are also characterized by a fast rise time, which contrasts with a slow decay (see Fig. 26).

After these individual signals, glioma cell population remains relatively silent for 3-4 minutes after which the cells initiate a strong electrical activity as shown in Fig. 27. For the first 500 seconds the signals are not periodic. The signal amplitude varies between 3 and 6 µV (peak-to-peak). This activity shows 3 strong signals which precede a quasi-periodic burst of

signals. In the quasi-periodic burst the signals have an amplitude of 2 μV (peak-to-peak) embedded in a noise level of 0.2 μV. The burst last for 500 seconds and it abruptly stops.

Fig. 28, Fig. 29 and Fig. 30 show detailed views of the signals. The individual signal shown in Fig. 30 is characterized by an initial negative variation on the voltage with a duration of 5-6 seconds. This negative variation is then followed by a fast transition to a positive variation almost symmetrical in respect to the steady state DC voltage value. The positive change in voltage then decays to the steady state in a time scale of 12-15 seconds.

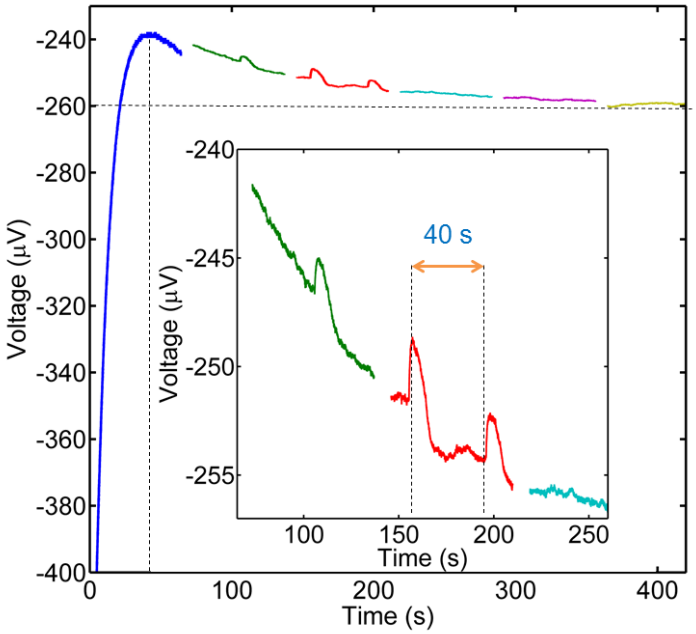

Fig. 26: Time dependence of the voltage at the electrode surface immediately after the application of a train of pulses. The inset shows a detail view of 3 broad signals.

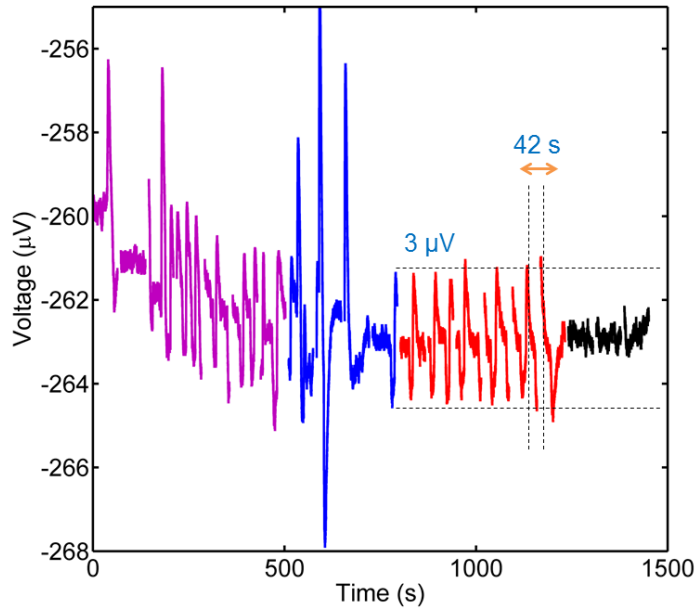

Fig. 27: Onset of an activity burst after the application of a train of pulses.

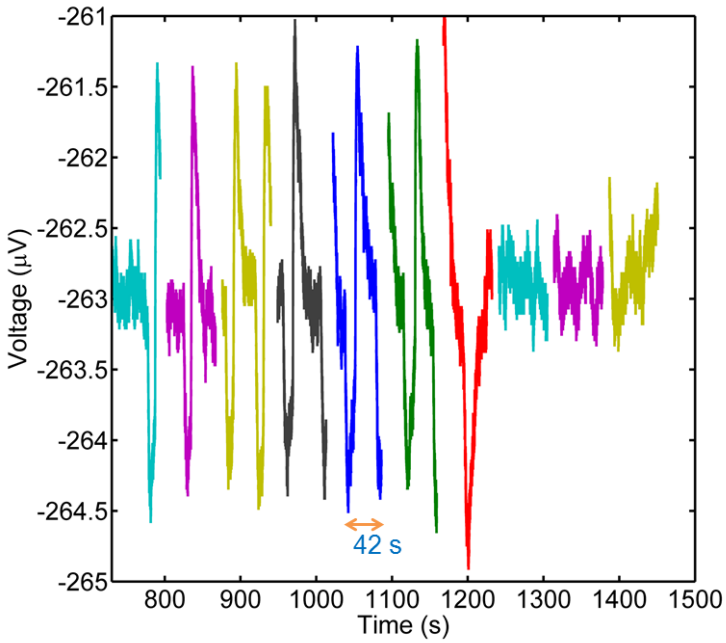

Fig. 28: Detail view of the activity burst, the signals have a bipolar shape with a period of 42 seconds.

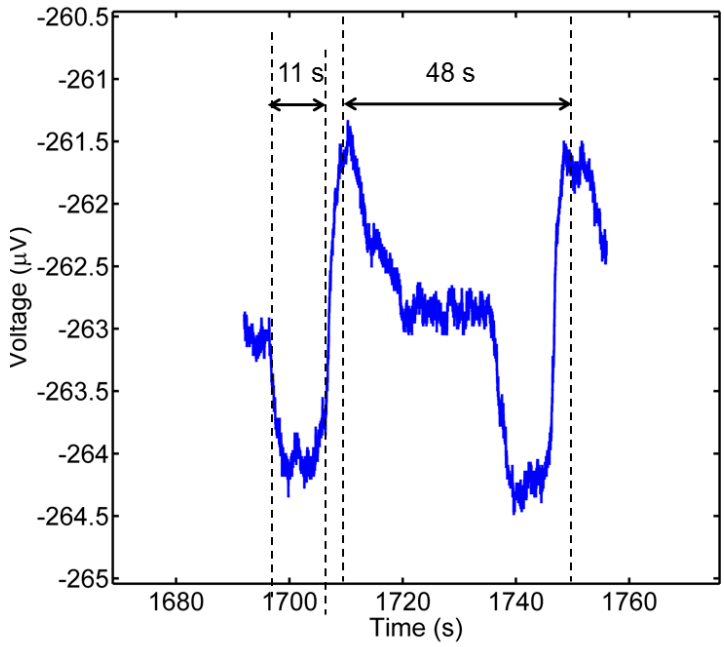

Fig. 29: Detailed view of two consecutive signals recorded in the quasi-periodic activity burst.

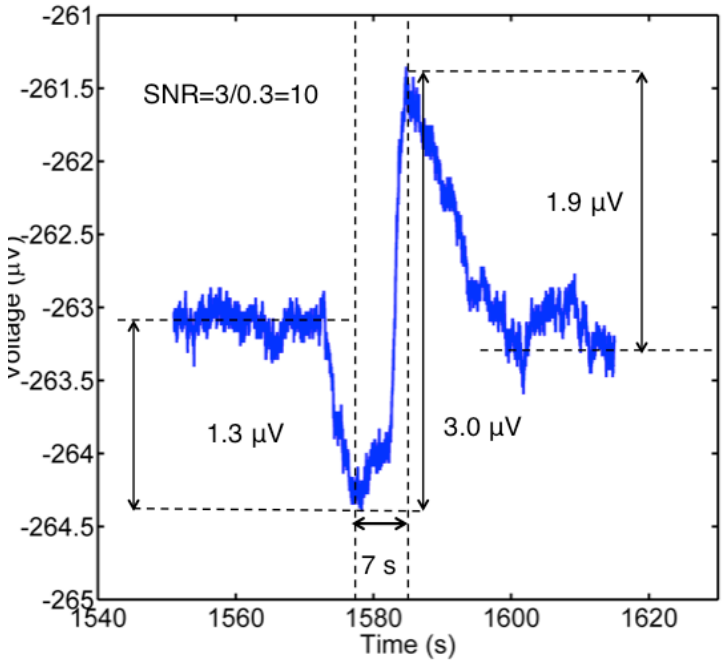

Fig. 30: Detailed view of a single signal recorded in the quasi-periodic activity burst.

5.3 Discussion

The findings show that the glioma cells respond to an external electrical stimulus. The application of a train of voltage pulses causes a transient response with an overshooting process that is not predicted by the simple double-layer equivalent circuit. The transient response occurs in a time-scale of several minutes, suggesting that the mechanism is not pure electronic. We propose that the voltage causes a large displacement of charged species near the gold/electrolyte interface. The ionic movement may cause the overshooting process. The analysis of the signal shape indicates that a negative variation (of voltage) is immediately followed by a positive change of equal magnitude. This suggest some charge balance mechanism.

6 Extracellular signal recordings: AM and FM communication patterns

Abstract

This chapter presents spontaneous extracellular activity recorded in primary astrocytes populations. The long term spontaneous activity show amplitude modulated (AM) patterns as well as frequency modulated (FM) patterns. These signal patterns are discussed on the terms of cellular communication networks in subpopulations of cells which get synchronized.

6.1 Introduction

All cells, not just excitable neurons and muscle, generate and receive bioelectrical signals encoded in changes in transmembrane potential and ion fluxes that change on a time-scale of seconds to days. These biophysical events are a crucial component of the cellular conversations that enable large-scale pattern formation and morphostasis. Cell used these electrical signals to regulate important events at the level of individual cell behavior, controlling cell number (proliferation and apoptosis), cell shape (orientation and outgrowth), cell position (migration and galvanotaxis) and cell differentiation (or de-differentiation), for migration regeneration repair and suppression of cancerous disorganization.

Signals, and hence information, can generally be transmitted either by amplitude (AM) or frequency (FM) modulation, as used, for example, in Telecommunications field. Both types of modulation are known to play a role in biology It is well know that cells sense external concentrations and, via biochemical signaling, respond by regulating the expression of target proteins. There are two main mechanisms by which the concentration can be encoded internally: amplitude modulation (AM), where the absolute concentration of an internal signaling molecule encodes the stimulus, and frequency modulation (FM), where the period between successive bursts represents the stimulus. Both mechanisms have been observed in biological systems.

In this chapter we show slow electrical oscillations that follow AM and FM patterns without any external stimulation. The AM and FM signal patterns are discussed in terms of a synchronized activity in distinct subpopulations of cells.

6.2 Experimental

The sensing electrodes used consist of two co-planar, parallel gold tracks on the upper surface of a thermal oxidized silicon wafer. Gold electrodes were deposited by thermal evaporation. The electrode shapes and dimensions are according to the labels in Fig. 31, where W is electrode length, L the inter-electrode distance and D the electrode depth. Each microelectrode has a total number of 10 interdigitated fingers and each finger has a length of 1000 μm. The total electrode length is 10xW=10.000μm, L=20μm, and D=15μm. The total active sensing area is 150.000 μm^2. These devices were provided by PHILIPS research labs in Eindhoven (NL). On top of the interdigitated electrodes a PMMA compartment is glued that can be filled with cells and culture medium. The well is loosely covered with a lid to prevent

evaporation of the medium. The system assures the presence of enough cell culture medium to keep the cells viable over more than 24 hours without medium change. Fig. 31 (a) shows a schematic diagram of the electrode and Fig. 31(b) shows a photograph of the complete sensing device. Fig. 31 (b) shows a schematic diagram of the electrode, with a top well and pads for the electrical connections.

6.3 Animals

C57Bl6/J mice were kept in our animal facility, with controlled temperature (21 ± 1ºC) and humidity (55%), with food and water *ad libitum* in a 12h dark/light cycle. The experiments were performed in accordance with institutional and European guidelines (2010/63/EU) for the care and use of laboratory animals. Both the Portuguese law (DL 113/2013) and the European law (directive 2010/63/EU) state that obtaining tissue for cell cultures without actually performing any procedures in a laboratory animal does not require an official approval from the competent authority (Direcção Geral de Alimentação e Veterinária, DGAV), since no procedures are performed (the law understands that a procedure is the equivalent of provoking discomfort in an animal similar to a needle piercing the skin), only that the process of sacrificing animals is performed by a licensed user. The animals were kept in our licensed animal house facility. We state that this study was performed according to the guidelines, established by our institute, and by law.

6.4 Primary astrocyte cultures

Primary mixed glial cultures were obtained from new-born C57Bl6/J mice with 0-3 days [55]. Briefly, after decapitation the brains were removed and the meninges and cerebellum were discarded. Brain tissue was then mechanically dissociated and enzymatically digested (0.1% trypsin and 0.001% DNase I, 20 min at 37°C). Cells were seeded in 25 cm^2 or 75 cm^2 flasks coated with poly-L-lysine, at a density of 0.2 x 10^6 cells/cm^2, and cultured in D-MEM/F12 with GlutaMAX^{TM}-I supplemented with 10% fetal bovine serum, 0.25% gentamicin and 0.25 ng/ml M-CSF, at 37°C and 95% air / 5% CO_2, in a humidified incubator. Culture medium was replaced every 4 days and confluency was achieved after 15 days, *in vitro*. Microglia and olidendrocyte precursor cells were removed by vigorous shaking, affording an astrocytes culture with around 98% of purity. After detachment of microglia cells, astrocytes were trypsinized (0.25%, 20 min at 37°C) and seeded on the electronic devices. The cell culture

medium used during electrical measurements is the same as used for culturing the cells. An aliquot of 200.000 cells per cm^2 was transferred to the well and was placed in an incubator (Thermo Scientific, Midi 40). Prior to cell deposition, the micro-structured electrodes were sterilized by UV treatment and the electrodes were coated with poly-L-lysine to promote cell adhesion. The cells were maintained in an incubator at 37 ºC, keeping a humidified atmosphere with 5% of CO_2. The system assures the presence of enough cell culture medium to keep the cells viable over more than 24 hours without medium change. Cell numbers and viability was assessed using a Neubauer chamber-based trypan blue live/dead exclusion assay. Images of the astrocytes cultures were recorded using a phase contrast microscopy method using an Axiovert 40 CFL microscope from Zeiss.

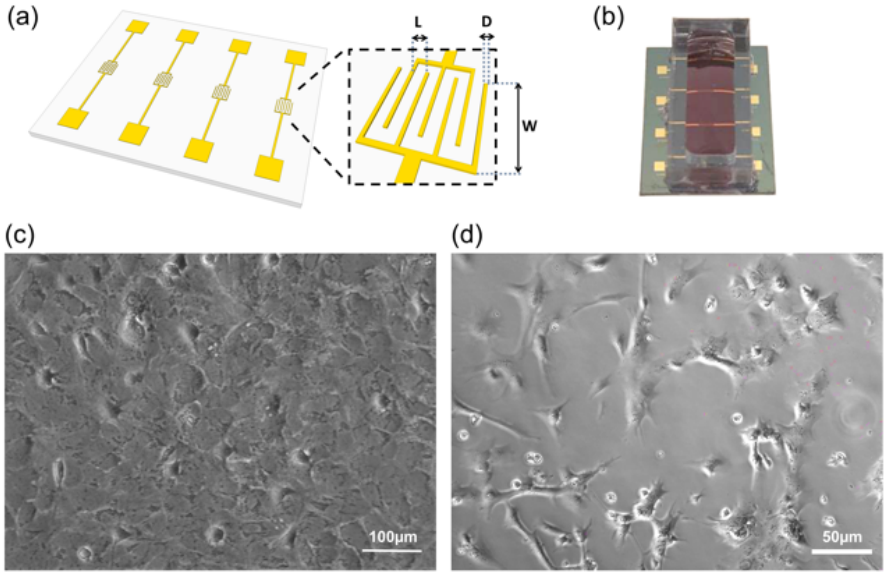

Fig. 31: Sensing devices and cells used in this study. (a) Schematic diagram of an interdigitated electrode fabricated on a silicon wafer. Device dimensions are W=1000µm, L=20µm, and D=15µm. (b) Schematic diagram of the device mounted in a vessel with electrical connections. (c) and (d) are photographs of astrocytes populations. The estimated cell confluence is 90% for the cells in (c) and 70% for the cells in photograph (d). These images were recorded using phase contrast microscopy method.

6.5 Electrical Measurements

The entire experimental set-up was specifically designed for ultrasensitive detection. External interference was minimized through the use of a Faraday cage and low noise cables. Extracellular voltage measurements were carried out using a low-noise voltage amplifier (SR 560, Stanford Research) and a dynamic signal analyzer (35670A, Agilent) (See chapter 5, Fig. 25). To minimize drift, the current amplifier is calibrated and the set-up is stabilized for at least two hours before measuring. The current was recorded as a function of time by using zero bias on the electrodes. Small-signal impedance measurements were carried out using a RCL meter Fluke PM 6306.

6.6 Results

Fig. 32 (a) shows a typical time trace of astrocytes spontaneous activity. After 1-2 hours of cell seeding on the device, astrocytes exhibit spontaneous weak signals. These early stage signals are approximately 1.5 μV in amplitude and they appear in clusters of a few (<10) discrete signals. With time, the astrocyte overall activity evolves to a new type of spontaneous activity, which is characterized by bursts of quasi-periodic signals and an increase of the signal magnitude. These bursts are briefly interrupted by shorter periods where both the signal rate and magnitude are lower. Bursts are characterized by a slow rise in signal amplitude until a maximum is reached. After attaining the maximum, the pattern decays following time dependence similar to the one followed during the rise in amplitude. This behavior originates symmetric signal patterns modulated in amplitude. We refer to these patterns as amplitude modulated (AM) bursts. Several AM burst are visible on Fig. 32 (a). The temporal duration of an AM burst may vary from several minutes to hours.

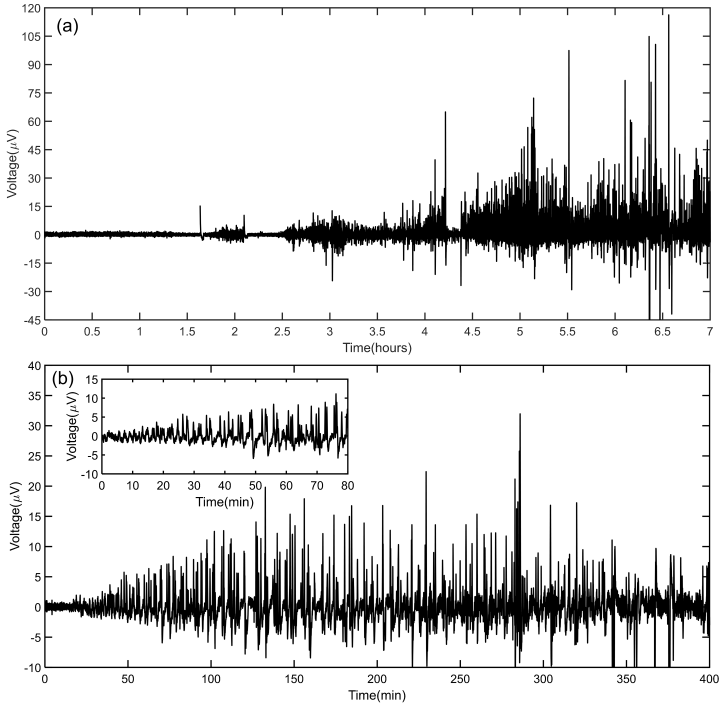

Fig. 32: Electrical signals recorded in astrocytes populations. (a) An overview of a long-term recording of astrocyte population activity, with different amplitude modulated (AM) bursts of activity. (b) a detailed view of a long AM burst lasting for 400 minutes. The inset shows a detailed view of the early stage of AM burs.

Fig. 33 shows a typical AM modulated burst. A burst can be characterized by its duration and by its peak in amplitude. The burst is fitted with a smooth curve that outlines the extremes. This is called the AM envelope. From this envelope we estimate the AM envelope peak. Fig. 33 shows an AM burst of spontaneous activity with duration of 100 minutes. The estimated AM envelope peak is 74.5 μV. The AM envelope was determined using the spline interpolation over the local maxima separated by at least 60 seconds for the higher amplitude envelope and by 100 seconds for the lower amplitude envelope, on Fig. 33.

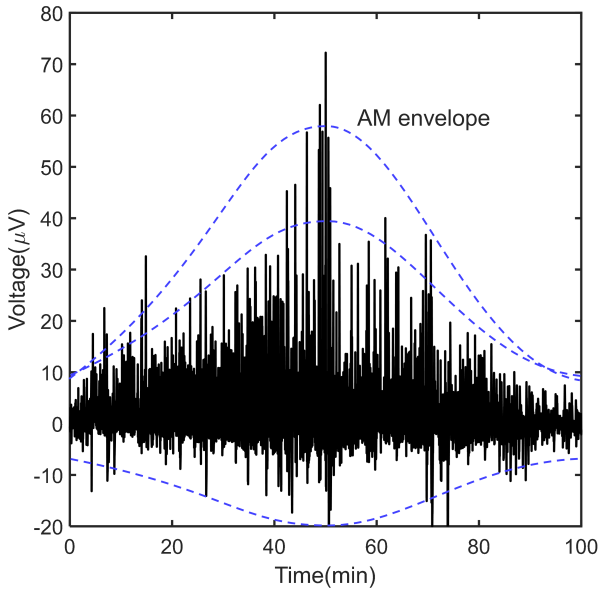

Fig. 33: Typical AM modulated burst lasting for 100 minutes.

During long-term recordings, different AM burst may not be well separated on time. Often is observed that some burst they mix or superimpose as shown in Fig. 34. The possible biological origin of this process will be discussed later. We will put forward a speculative explanation related with the existence of several subpopulations of cells generating individual patterns of communication.

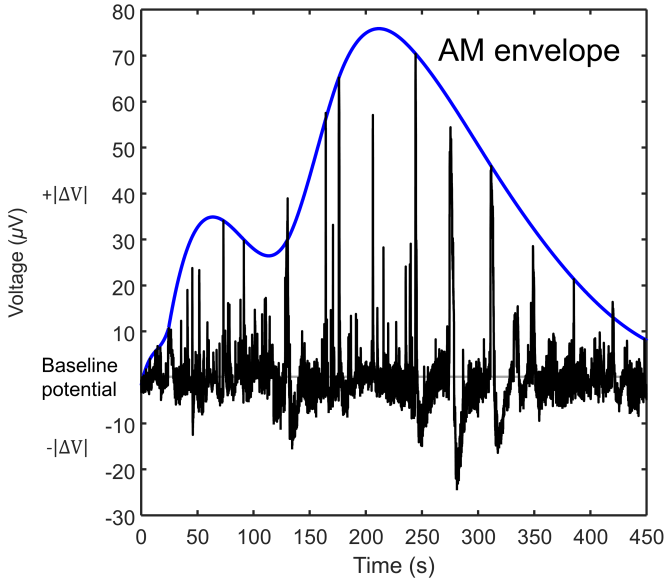

Fig. 34: Intermix between two AM bursts.

Fig. 36 shows an example of a second type of burst also frequently recorded during our experiments. These bursts are characterized by a frequency modulation (FM). At the onset of

the burst, the frequency rises fast up to 15 spikes/min and then begins to decrease slowly until the signals disappear. The decrease in frequency can vary from a few minutes up to a half-hour. The progressive frequency shift to lower frequencies (red shift) is not necessary accompanied by a decrease in signal amplitude, as observed in the AM modulation discussed above. The FM modulation is clearly observed in Fig. 35 for t>12 minutes. When all the signals in Fig. 35 are analyzed and the number of spikes per minute is represented in a form of a bar plot, the red shift in frequency becomes clearly visible.

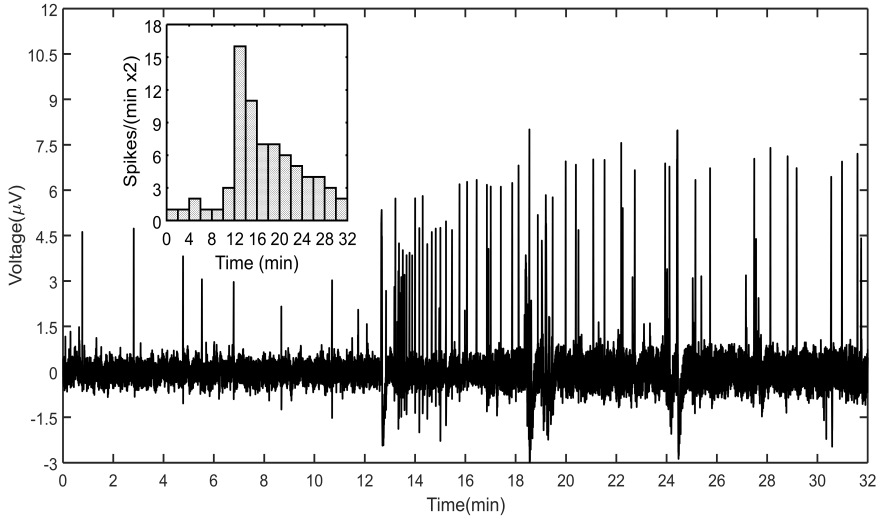

Fig. 35: Signal pattern with frequency modulation. Time trace showing a frequency modulation for t > 12 minutes. The barplot in the inset shows that the signal rate decreases with time (frequency modulation).

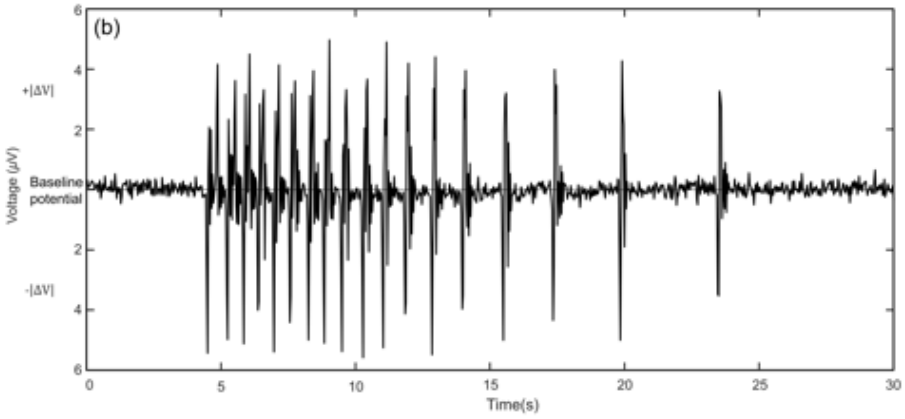

Fig. 36: Detailed view of a FM modulation recorded in a cluster of relatively fast signals.

AM and FM modulation may co-exist simultaneously. A typical example is shown in

Fig. 37. As already discussed above, this may be due to two distinct subpopulations of cells generation. One subpopulation is generating an AM burst whereas the other subpopulation is generating the FM burst. Both signal patterns were recorded simultaneously.

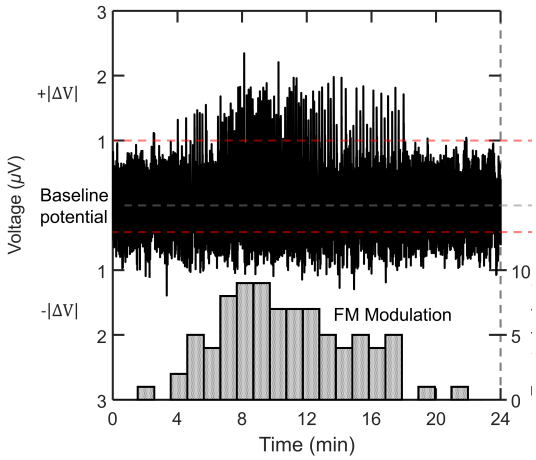

Fig. 37: Time trace of cell signals showing the simultaneous co-existence of an AM and FM modulation.

6.7 Discussion

A large area electrode cannot resolve single cell signals; the recorded trace reflects the combined activity an astrogial ensemble. If a large number of individual cells generate independent signals obeying to the same statistic then, according to the central limit theorem, the resulting activity resembles noise since the distribution of the average of a large number of independent, identically distributed variables will be approximately normal. The central limit theorem states that, in most situations when independent random variables, which in this case are signals from cells, are added, their properly normalized sum tends to a normal distribution. To explain the observation of discrete, temporally structured signals, several hypotheses may be considered. An obvious one is that the population of cells is synchronized by a biological signaling process (pacemaker mechanism, just as in a cardiac beating signal where individual signals sum up into an averaged discrete signal). However, a synchronized population of cells is not expected to generate modulating patterns. To explain the existence of AM or FM like modulated patterns we need to consider the existence of sub-populations of cells. A sub-population of cells is seen here as a relatively small number of cells that are synchronized. For the following reasoning a sub-population, in the limit, can be a single cell. These sub-populations may be sparse and distributed over the entire electrode area and generate signals

with slightly different frequencies and phases, giving rise to patterns with an AM and FM like modulation. These modulations are known, and have been proposed as a way to encode biological information [56]. Previous studies have shown that the modulations occur in response to chemical stimuli [57] and have been recorded in distinct time traces.

6.8 Conclusions

This study has demonstrated that extracellular electrophysiological measurements show a richness of detail never reported before using imaging methods. For example, electrical signals rarely start abruptly. Once the signals start, they gently increase in amplitude and rate, showing that an increasing number of cells get synchronized or are somehow correlated.
We have shown signal patterns with FM and AM modulation that repeat in a quasi-periodic trend.

7 Conclusions and suggestions for further work

The technology developments to perform electrophysiological measurements have been focused on electrogenic cells, such as muscle cells or neurons. In contrast, the research presented in this thesis aims to measure populations of non-electrogenic cells. Astrocytes are one example of this type of cells. Astrocytes generate signals that are typical 1000 times weaker and 1000 times slower than an action potential generated by a neuron. An action potential has duration of a few milliseconds and an amplitude that can easily reach millivolts. Astrocytes signals presented in this thesis are in the range of microvolts and they can last for periods of time of several seconds. To record these signals we have develop electrodes that have a very low intrinsic thermal noise. Our strategy was twofold, (i) increase the physical area and (ii) made the surface micro structured to promote a more intimate interaction of the electrode with cells.

Our experimental approach enables the study of astrocyte electrophysiology in a totally non-invasive manner, with a high temporal resolution, and over extended periods of time. The advantages of the method were demonstrated by showing a variety of spontaneous signals. Furthermore, newly revealed signals and signal patterns, which had remained inaccessible using conventional imaging and patch-clamp methods, have also emerged.

This study has also demonstrated that extracellular electrophysiological measurements show a richness of detail never reported before using imaging methods. For example, once the signals start, they gently increase in amplitude and rate, showing that an increasing number of cells get synchronized or are somehow correlated. The temporal dependence of the cells synchronization process can be followed in real time. This is a feature not entirely perceived using fluorescence techniques.

Extracellular electrical recordings can be performed over periods as long as a week, this enabling the observation of signals patterns that could not be accurately recorded using conventional imaging methods. We have shown signal patterns with FM and AM modulation that repeat in a quasi-periodic trend. These modulations have been proposed as a way to encode biological information. Previous studies have shown that the modulations occur in response to chemical stimuli and have been recorded in distinct time traces. To the best of our knowledge, this work provides the first report on FM and AM signal modulations occurring spontaneously, monitored in real time in a single time trace.

The AM and FM patterns deserve now an intense analysis. It is important to know how frequent these patterns appear? What is the biological process involved in generating the patterns? how can they be trigger or inhibited. There is all range of experiments that needs to be carried out to shed some light on this fascinating bioelectrical communication protocol.

8 References

[1] L. Galvani, "De viribus electricitatis in motu muscularis commentarius," *Bononiensi Sci. Artium Inst. atque Acad. Comment.*, vol. 7, pp. 363–418, 1791.

[2] A. L. Hodgkin and A. F. Huxley, "A quantitative description of membrane current and its application to conduction and excitation in nerve," *Bull. Math. Biol.*, vol. 52, no. 1–2, pp. 25–71, 1990.

[3] D. W. Kennard, "Glass microcapillary electrodes used for measuring potential in living tissues," *Electron. Appar. Biol. Res.*, pp. 534–567, 1958.

[4] E. Neher, B. Sakmann, and J. H. Steinbach, "The extracellular patch clamp: A method for resolving currents through individual open channels in biological membranes," *Pflügers Arch. Eur. J. Physiol.*, vol. 375, no. 2, pp. 219–228, 1978.

[5] M. E. J. Obien, K. Deligkaris, T. Bullmann, D. J. Bakkum, and U. Frey, "Revealing neuronal function through microelectrode array recordings," *Front. Neurosci.*, vol. 8, no. JAN, p. 423, Jan. 2015.

[6] D. A. Robinson, "The electrical properties of metal microelectrodes," *Proc. IEEE*, vol. 56, no. 6, pp. 1065–1071, 1968.

[7] M. Grattarola and S. Martinoia, "Modeling the Neuron-Microtransducer Junction: From Extracellular to Patch Recording," *IEEE Trans. Biomed. Eng.*, vol. 40, no. 1, pp. 35–41, 1993.

[8] R. Weis and P. Fromherz, "Frequency dependent signal transfer in neuron transistors," *Phys. Rev. E*, vol. 55, no. 1, pp. 877–889, 1997.

[9] J. R. Buitenweg, W. L. C. Rutten, and E. Marani, "Extracellular stimulation window explained by a geometry-based model of the Neuron-electrode contact," *IEEE Trans. Biomed. Eng.*, vol. 49, no. 12, pp. 1591–1599, Dec. 2002.

[10] V. Thakore, P. Molnar, and J. J. Hickman, "An optimization-based study of equivalent circuit models for representing recordings at the neuron-electrode interface," *IEEE Trans. Biomed. Eng.*, vol. 59, no. 8, pp. 2338–2347, 2012.

[11] S. Ingebrandt, C. K. Yeung, M. Krause, and A. Offenhäusser, "Neuron-transistor coupling: Interpretation of individual extracellular recorded signals," *Eur. Biophys. J.*, vol. 34, no. 2, pp. 144–154, 2005.

[12] N. Joye, A. Schmid, and Y. Leblebici, "A cell-electrode interface noise model for high-density microelectrode arrays," in *Proceedings of the 31st Annual International Conference of the IEEE Engineering in Medicine and Biology Society: Engineering the Future of Biomedicine, EMBC 2009*, 2009, pp. 3247–3250.

[13] M. R. Ward, *Electrical Engineering Science*. McGraw-Hill, 1971.

[14] P. J. Rousche, D. S. Pellinen, D. P. Pivin, J. C. Williams, R. J. Vetter, and D. R. Kipke, "Flexible polyimide-based intracortical electrode arrays with bioactive capability," *IEEE Trans. Biomed. Eng.*, vol. 48, no. 3, pp. 361–370, 2001.

[15] S. Takeuchi, T. Suzuki, K. Mabuchi, and H. Fujita, "3D flexible multichannel neural probe array," *J. Micromechanics Microengineering*, vol. 14, no. 1, pp. 104–107, 2004.

[16] A. Blau *et al.*, "Flexible, all-polymer microelectrode arrays for the capture of cardiac and neuronal signals," *Biomaterials*, vol. 32, no. 7, pp. 1778–1786, Mar. 2011.

[17] M. Sessolo *et al.*, "Easy-to-fabricate conducting polymer microelectrode arrays," *Adv. Mater.*, vol. 25, no. 15, pp. 2135–2139, 2013.

[18] M. P. Maher, J. Pine, J. Wright, and Y. C. Tai, "The neurochip: A new multielectrode device for stimulating and recording from cultured neurons," *J. Neurosci. Methods*, vol. 87, no. 1, pp. 45–56, 1999.

[19] G. Jing, Y. Yao, M. Gnerlich, S. Perry, and S. Tatic-Lucic, "Towards a multi-electrode

array (MEA) system for patterned neural networks," in *Procedia Chemistry*, 2009, vol. 1, no. 1, pp. 329–332.
[20] B. J. Dworak and B. C. Wheeler, "Novel MEA platform with PDMS microtunnels enables the detection of action potential propagation from isolated axons in culture.," *Lab Chip*, vol. 9, no. 3, pp. 404–10, 2009.
[21] M. G. Schrlau, N. J. Dun, and H. H. Bau, "Cell electrophysiology with carbon nanopipettes," *ACS Nano*, vol. 3, no. 3, pp. 563–568, 2009.
[22] K. D. Wise, "Silicon microsystems for neuroscience and neural prostheses," *IEEE Engineering in Medicine and Biology Magazine*, vol. 24, no. 5. pp. 22–29, 2005.
[23] F. Heer *et al.*, "Single-chip microelectronic system to interface with living cells," *Biosens. Bioelectron.*, vol. 22, no. 11, pp. 2546–2553, May 2007.
[24] M. Willemin, "Optical characterization methods for solid-state image sensors," *Opt. Lasers Eng.*, vol. 36, no. 2, pp. 185–194, 2001.
[25] L. Berdondini *et al.*, "High-density electrode array for imaging in vitro electrophysiological activity," *Biosens. Bioelectron.*, vol. 21, no. 1, pp. 167–174, 2005.
[26] K. D. Wise, J. B. Angell, and A. Starr, "An Integrated-Circuit Approach to Extracellular Microelectrodes," *IEEE Trans. Biomed. Eng.*, vol. BME-17, no. 3, pp. 238–247, 1970.
[27] P. Bergveld, "Short Communications: Development of an Ion-Sensitive Solid-State Device for Neurophysiological Measurements," *IEEE Trans. Biomed. Eng.*, vol. BME-17, no. 1, pp. 70–71, 1970.
[28] P. Bergveld, "Development, operation, and application of the ion-sensitive field-effect transistor as a tool for electrophysiology.," *IEEE Trans. Biomed. Eng.*, vol. 19, no. 5, pp. 342–351, 1972.
[29] W. H. Baumann, M. Lehmann, A. Schwinde, R. Ehret, M. Brischwein, and B. Wolf, "Microelectronic sensor system for microphysiological application on living cells," *Sensors Actuators, B Chem.*, vol. 55, no. 1, pp. 77–89, 1999.
[30] M. Lehmann *et al.*, "Non-invasive measurement of cell membrane associated proton gradients by ion-sensitive field effect transistor arrays for microphysiological and bioelectronical applications," *Biosens. Bioelectron.*, vol. 15, no. 3–4, pp. 117–124, 2000.
[31] K. Shimada, M. Yano, K. Shibatani, Y. Komoto, M. Esashi, and T. Matsuo, "Application of catheter-tip i.s.f.e.t. for continuousin vivo measurement," *Med. Biol. Eng. Comput.*, vol. 18, no. 6, pp. 741–745, 1980.
[32] H. Ecken, S. Ingebrandt, M. Krause, D. Richter, M. Hara, and A. Offenhäusser, "64-channel extended gate electrode arrays for extracellular signal recording," in *Electrochimica Acta*, 2003, vol. 48, no. 20–22, pp. 3355–3362.
[33] S. Meyburg *et al.*, "N-Channel field-effect transistors with floating gates for extracellular recordings," *Biosens. Bioelectron.*, vol. 21, no. 7, pp. 1037–1044, 2006.
[34] A. Cohen, M. E. Spira, S. Yitshaik, G. Borghs, O. Shwartzglass, and J. Shappir, "Depletion type floating gate p-channel MOS transistor for recording action potentials generated by cultured neurons," *Biosens. Bioelectron.*, vol. 19, no. 12, pp. 1703–1709, 2004.
[35] J. T. Robinson, M. Jorgolli, and H. Park, "Nanowire electrodes for high-density stimulation and measurement of neural circuits.," *Front. Neural Circuits*, vol. 7, no. March, p. 38, 2013.
[36] B. P. Timko, T. Cohen-Karni, G. Yu, Q. Qing, B. Tian, and C. M. Lieber, "Electrical recording from hearts with flexible nanowire device arrays," *Nano Lett.*, vol. 9, no. 2, pp. 914–918, 2009.
[37] E. W. Keefer, B. R. Botterman, M. I. Romero, A. F. Rossi, and G. W. Gross, "Carbon nanotube coating improves neuronal recordings," *Nat. Nanotechnol.*, vol. 3, no. 7, pp. 434–439, Jul. 2008.

[38] A. Mazzatenta *et al.*, “Interfacing Neurons with Carbon Nanotubes: Electrical Signal Transfer and Synaptic Stimulation in Cultured Brain Circuits,” *J. Neurosci.*, vol. 27, no. 26, pp. 6931–6936, Jun. 2007.
[39] M. Shein *et al.*, “Engineered neuronal circuits shaped and interfaced with carbon nanotube microelectrode arrays,” *Biomed. Microdevices*, vol. 11, no. 2, pp. 495–501, Apr. 2009.
[40] S. M. Richardson-Burns, J. L. Hendricks, and D. C. Martin, “Electrochemical polymerization of conducting polymers in living neural tissue,” *J. Neural Eng.*, vol. 4, no. 2, pp. L6–L13, Jun. 2007.
[41] T. Nyberg, A. Shimada, and K. Torimitsu, “Ion conducting polymer microelectrodes for interfacing with neural networks,” *J. Neurosci. Methods*, vol. 160, no. 1, pp. 16–25, 2007.
[42] P. Leleux *et al.*, “Conducting Polymer Electrodes for Electroencephalography,” *Adv. Healthc. Mater.*, vol. 3, no. 4, pp. 490–493, 2014.
[43] D. Khodagholy *et al.*, “In vivo recordings of brain activity using organic transistors,” *Nat. Commun.*, vol. 4, p. 1575, Mar. 2013.
[44] N. C. Hogan, G. Talei-Franzesi, O. Abudayyeh, A. Taberner, and I. Hunter, “Low-cost, flexible polymer arrays for long-term neuronal culture.,” *Conf. Proc. ... Annu. Int. Conf. IEEE Eng. Med. Biol. Soc. IEEE Eng. Med. Biol. Soc. Annu. Conf.*, vol. 2012, pp. 803–6, Aug. 2012.
[45] R. A. Green, N. H. Lovell, G. G. Wallace, and L. A. Poole-Warren, “Conducting polymers for neural interfaces: Challenges in developing an effective long-term implant,” *Biomaterials*, vol. 29, no. 24–25, pp. 3393–3399, 2008.
[46] R. Gerwig *et al.*, “PEDOT–CNT Composite Microelectrodes for Recording and Electrostimulation Applications: Fabrication, Morphology, and Electrical Properties,” *Front. Neuroeng.*, vol. 5, no. May, p. 8, 2012.
[47] U. A. Aregueta-Robles, A. J. Woolley, L. A. Poole-Warren, N. H. Lovell, and R. A. Green, “Organic electrode coatings for next-generation neural interfaces.,” *Front. Neuroeng.*, vol. 7, no. May, p. 15, 2014.
[48] Y. Fang, X. Li, and Y. Fang, “Organic bioelectronics for neural interfaces,” *J. Mater. Chem. C*, vol. 3, no. 25, pp. 6424–6430, 2015.
[49] A. Fendyur, N. Mazurski, J. Shappir, and M. E. Spira, “Formation of essential ultrastructural interface between cultured hippocampal cells and gold mushroom-shaped MEA- toward ‘ IN-CELL ’ recordings from vertebrate neurons,” vol. 4, no. December, pp. 1–14, 2011.
[50] A. Fendyur and M. E. Spira, “Toward on-chip , in-cell recordings from cultured cardiomyocytes by arrays of gold mushroom-shaped microelectrodes,” vol. 5, no. August, pp. 1–10, 2012.
[51] M. Cerquido, “Fabrication of biocompatible gold mushrooms-shaped microelectrodes for the recording of neuronal signals.” 2016.
[52] M. C. R. Medeiros *et al.*, “An electrical method to measure low-frequency collective and synchronized cell activity using extracellular electrodes,” *Sens. Bio-Sensing Res.*, vol. 10, pp. 1–8, Sep. 2016.
[53] W. Franks, I. Schenker, P. Schmutz, and A. Hierlemann, “Impedance characterization and modeling of electrodes for biomedical applications,” *IEEE Trans. Biomed. Eng.*, vol. 52, no. 7, pp. 1295–1302, 2005.
[54] P. M. C. Inacio *et al.*, “Bioelectrical Signal Detection Using Conducting Polymer Electrodes and the Displacement Current Method,” *IEEE Sens. J.*, vol. 17, no. 13, 2017.
[55] B. P. Carreira *et al.*, “Nitric oxide from inflammatory origin impairs neural stem cell proliferation by inhibiting epidermal growth factor receptor signaling.,” *Front. Cell.*

Neurosci., vol. 8, no. October, p. 343, Oct. 2014.
[56] M. J. Berridge, M. D. Bootman, and H. L. Roderick, “Calcium: Calcium signalling: dynamics, homeostasis and remodelling,” *Nat. Rev. Mol. Cell Biol.*, vol. 4, no. 7, pp. 517–529, Jul. 2003.
[57] L. Pasti, A. Volterra, T. Pozzan, and G. Carmignoto, “Intracellular Calcium Oscillations in Astrocytes : A Highly Plastic , Astrocytes In Situ,” vol. 17, no. 20, pp. 7817–7830, 1997.